Impact of Patient-Specific Inflow Boundary Conditions and Concentration Initialization on Hemodynamics and Low-Density Lipoproteins Transport in the Thoracic Aorta

Politecnico di Torino
Department of Mechanical and Aerospace Engineering
Doctoral Program in Bioengineering and Medical-Surgical Sciences
2014 - 2017

Impact of Patient-Specific Inflow Boundary Conditions and Concentration Initialization on Hemodynamics and Low-Density Lipoproteins Transport in the Thoracic Aorta

Giuseppe De Nisco

Tutor:
Prof. Umberto Morbiducci

Doctoral Dissertation - Doctoral Program in
Bioengineering and Medical-Surgical Sciences (30th Cycle)

Impact of Patient-Specific Inflow Boundary Conditions and Concentration Initialization on Hemodynamics and Low-Density Lipoproteins Transport in the Thoracic Aorta

Giuseppe De Nisco
******

Supervisor:
Prof. Umberto Morbiducci, Supervisor

Doctoral Examination Committee:
Dott. Mauro Grigioni, Referee, Istituto Superiore di Sanità
Dott. Michele Conti, Referee, Università degli Studi di Pavia

Politecnico di Torino 2014/2017

Declaration

I hereby declare that, the contents and organization of this dissertation constitute my own original work and does not compromise in any way the rights of third parties, including those relating to the security of personal data.

Giuseppe De Nisco

2017

* This dissertation is presented in partial fulfillment of the requirements for **Ph.D. degree** in the Graduate School of Politecnico di Torino (ScuDo).

I would like to dedicate this thesis to all scientists and researchers around the World, daily fighting to solve or explain mysteries of science.

Vorrei dedicare questa tesi a tutti gli scienziati e ricercatori del Mondo, che "lottano" quotidianamente per risolvere o spiegare i misteri della scienza.

Acknowledgments

First of all, at the end of this course, I would like to thank Professor Umberto Morbiducci for giving me the opportunity to do this work. I am deeply grateful to him for having encouraged my research activity during these three years, for sharing his knowledge and experiences with me, for always giving me constructive and critical suggestions and clarifications. The passion and dedication with which he conducts his research activity and his way of leading our research group have always stimulate me to improve my knowledge and to face occurred activity obstacles with the freedom to elaborate and experiment with new methods, allowing me to learn from my mistakes. I will always be grateful for showing me the difference between a leader and a boss.

I am also deeply grateful to Dr. Diego Gallo for his precious support, both scientific and gastronomic. Good food always lead to good ideas.

I would like to thank my family, which is ready to follow and accompany me, from a distance, in each phase of my studies, and my partner in life, Francesca, whom is able to understand

me and encourage my activity. She is able to change my day with just a smile.

I wish to thank also all my colleagues and friends of the 5° floor (including people in lab). Thanks to Gianpaolo, sidekick from the first to the last day of this scientific course; thanks to Andrès, Seffino and Seffo to have made me feel lighter, despite hard working days, and to Chef Paoletta to have made me feel heavier. I am happy to be part of this smart, hungry, crazy, noisy group.

I am very proud to be BoB, since four years.

Short Curriculum Vitae

Full name	GIUSEPPE **DE NISCO**
Date and place of birth	2/12/1989 - Benevento, Italy
Nationality	Italian
Residence	Venticano (AV) - 83030 - Italy
e-mail	*giuseppe.denisco@polito.it*

Post-secondary Education _____

Biomedical Engineering (110/110 *e lode*)
Università Federico II - Naples (Italy)
27/09/2008 - 23/01/2012 B.Sc.

Biomedical Engineering (110/110 *e lode*)
Politecnico di Torino (Italy)
09/03/2012 - 23/07/2014 M.Sc.

Doctoral Program in Bioengineering and Medical-Surgical Sciences (30th Cycle)
Politecnico di Torino - Università degli Studi di Torino (Italy)
01/11/2014 - 31/10/2017 Ph.D. Candidate

International Experience _____

Analysis of image-based computational hemodynamic models of pigs' coronary arteries.
Erasmus University Medical Center- Rotterdam (Netherlands)
September 2017

Publications _____

2016 Maffiodo, D.; De Nisco, G.; Gallo, D.; Audenino, A.; Morbiducci, U.; Ferraresi, C.
A reduced-order model-based study on the effect of intermittent pneumatic compression of limbs on the cardiovascular system.
Proceedings Of The Institution Of Mechanical Engineers. Part H, Journal Of Engineering In Medicine - Vol. 230(4): 279-87.

2018 De Nisco, G.; Zhang, P.; Calò, K.; Liu, X.; Ponzini, R.; Bignardi, C.; Rizzo, G.; Deng, X.; Gallo, D.; Morbiducci, U.
What is needed to make low-density lipoprotein transport in human aorta computational models suitable to explore links to atherosclerosis? Impact of initial and inflow boundary conditions.
Journal Of Biomechanics - Vol. 68: 33-42.

Conference _____

A model-based study of the effect of intermittent pneumatic compression of limbs on the cardiovascular system.
Poster Presentation

V Meeting of European Society of Biomechanics - Capitolo Italiano 2015 - Milan (Italy)
05/06/2015

On the impact of modeling assumptions in subject-specific hemodynamic simulations of low-density lipoproteins transport in aorta.
Oral Presentation
VI Meeting of European Society of Biomechanics - Capitolo Italiano 2016 - Naples (Italy)
22/06/2016

Impact of idealized versus measured velocity profiles in computational models of mass transport in the human aorta.
Poster Presentation
Summer Biomechanics, Bioengineering, Biotransport Conference 2016 - National Harbor, (MD, USA)
29/06/2016 - 02/07/2016

Influence of idealized versus measured velocity profiles on mass transfer in CFD modelsof thoracic aorta.
Oral Presentation
22nd Congress of the European Society of Biomechanics 2016 - Lyon (France)
10/07/2016 - 13/07/2016
Co-chair man of Biofluids Mechanics section

PC-MRI derived inlet boundary conditions in CFD models of Human aorta: uncertainty propagation.
Oral Presentation
Summer Biomechanics, Bioengineering and Biotransport Conference 2017 - Tucson (AZ, USA)
21/06/2017 - 24/06/2017

Physiological significance of helical flow in coronary arteries.
Poster Presentation
13th International Symposium on Biomechanics in Vascular Biology and Cardiovascular Disease - Atlanta (GA, USA)
12/04/2018 - 13/04/2018

Abstract

The complex hemodynamics observed in the human aorta make this district a site of election for an in depth investigation of the relationship between fluid structures, transport and patho-physiology. In fact, it is well known that hemodynamics play an important role in the mass transport of blood specimen, and in turn, in their transfer to the vascular wall and ultimately in the localization of vascular disease in areas of complex arterial flow. In particular, the accumulation of lipoproteins in the arterial intima is a hallmark of atherosclerosis. Low-density lipoproteins (LDL) are the most abundant atherogenic lipoproteins in plasma and high plasma levels of LDL are causally related to the development of atherosclerosis.

Advanced computational fluid dynamics coupled with medical imaging allows to combine the anatomical and hemodynamic inputs to realistic, fully personalized flow simulations to study local hemodynamics in arteries. Such an

approach represents an effective way when addressing the still open questions about the role of blood-side LDL transfer to the arterial wall in atherogenesis. In particular, personalized computational models have been proposed to study LDL blood-to-wall transfer in the aorta, a district of election for the study of the relationships between the intricate local hemodynamics, LDL transport and disease.

However, computational hemodynamics requires some assumptions that could affect the solutions of the equations governing blood flow and the aortic LDL transport and wall transfer. In previous studies of my research group, has been demonstrated that different strategies in applying boundary conditions (BCs) derived from phase-contrast MRI (PC-MRI) measurements could lead to different results in terms of distribution of near-wall and intravascular flow quantities. Additionally, a paucity of data characterizes the literature concerning the BCs and initial conditions (ICs) adopted to model LDL transport.

In this contest, my thesis project have been focalized in analysing the impact that different possible strategies of applying (1) PC-MRI measured data as inflow BCs, and (2) LDL concentration profiles as ICs, have on LDL blood-to-wall transfer modelling in the human aorta. Technically, two

different inflow BCs are generated, by imposing at the ascending aorta inflow PC-MRI measured 3D velocity profiles or idealized (flat) velocity profiles. In this way, the sensitivity of blood-to-wall LDL transfer to the inflow BC is explored, as the inflow BC influences LDL advective transport.

The impact of applied BC-IC strategies on LDL blood-to-wall transfer has been evaluated in terms of computational costs and LDL polarization profiles at the luminal surface. Moreover, by virtue of the reported high LDL concentration in correspondence of disturbed shear regions, here a co-localization analysis with areas exposed to atheroprone wall shear stress (WSS) phenotype has been conducted as a "physics consistency check".

The results of my research would contribute to clarify which is (1) the level of detail obtained from measured flow data to be used as inflow BC, and (2) the plausibility of hypotheses on LDL concentration to be used as IC strategy, to satisfactorily simulate mass transport/transfer in personalized complex hemodynamic models of human aorta.

Contents

List of Figures

List of Tables

A version of this manuscript has been published in:
De Nisco, G., Zhang, P., Calò, K., Liu, X., Ponzini, R., Bignardi, C., Rizzo, G., Deng, X., Gallo, D., Morbiducci, U. *What is needed to make low-density lipoprotein transport in human aorta computational models suitable to explore links to atherosclerosis? Impact of initial and inflow boundary conditions*.
Journal of Biomechanics - Vol. 68: 33-42, Feb. 2018.

Chapter 1

Introduction

1.1 Motivations of the thesis project

The cardiovascular system is an internal flow loop, divided in multiple branches where blood circulates. Physiological arterial blood flow is mainly laminar, with secondary flows generated at vessels' curves and branches. Arteries are able to adapt, vasodilating or vasoconstricting themselves, to different hemodynamic conditions of flow and pressure. The vascular response to hemodynamic environment can result in a normal adaptation or in pathological disease. In particular, an altered hemodynamics can cause and abnormal biological response, promoting the onset and the progression

of atherosclerotic disease, representing a major cause of death in the western world (Allender et al, 2008).

Atherosclerosis consists in the formation of a lipid-rich plaque at the vessel wall resulting, generally, in a reduction of the vascular lumen section and/or in a circulating thrombus formation. In particular, the narrowing of the arterial lumen (stenosis) can cause turbulence and reduce flow by means of viscous head losses and flow choking. The disease tends to localize in arterial districts characterized by branching and higher curvature where wall shear stress (WSS) and other hemodynamic features deviate from their normal spatial and temporal distribution in straight vessels (Nerem, 1995). Among several systemic and local proatherogenic factors, hemodynamic forces are large responsible for dictating with vessel are either susceptible or resistant to developing atherosclerosis. This high-susceptibility sites are found in vascular regions of low shear stress and oscillatory flow, characterized by “disturbed shear”.

Hemodynamics plays also an important role in the mass transport in the blood flow, and so, concerning atherosclerotic disease, in the low-density lipoproteins (LDL) blood transport and in them transfer to the vessel wall. LDL are, in fact, the most abundant atherogenic lipoproteins in plasma and high

plasma levels of LDL are causally related to the atherosclerosis development (Tarbell, 2003).

Because of the even higher interest in personalized computational hemodynamics as a supporting, predicting and clarifying tool to vascular disease investigation, in this thesis work the effect of several simplifying assumptions in patient-specific computational models of human thoracic aorta has been investigated. The complex hemodynamics characterizing the human aorta, in fact, make this district a site of election for an in-depth investigation of the relationship among fluid structures, transport and phato-physiology.

The motivation of this study is due to the cumbersomeness of protocol useful to obtain reliable estimations of LDL distribution at the vessel wall in modelling blood-side to wall LDL transfer. This paucity of data is limiting the establishment of rigorous computational hemodynamics protocols able to balance the trade-offs among the variety of in vivo data to be acquired, and the accuracy required by biological/clinical applications.

In this study, the impact of LDL concentration initialization (initial conditions, ICs) and inflow boundary conditions (BCs) on computational hemodynamics models of LDL blood-to-wall transfer in aorta has been analyzed. In

detail, in an image-based model of human aorta, two different inflow BCs are generated imposing subject-specific inflow 3D PC-MRI measured or idealized (flat) velocity profiles. For each simulated boundary condition, four different initial conditions for LDL concentration at the vessel wall are applied.

1.2 Anatomy of cardiovascular district

1.2.1 The cardiovascular system

The cardiovascular system consists of three main structures: the heart, the blood vessels and the blood; its function is providing the body tissues with oxygen and nutrients carried by the blood through the arteries, arterioles and capillaries, while the deoxygenated blood, full of unused nutrients and waste products, is sent back to the heart through the veins and venules.

Blood flow within downstream vessels is provided by heart pumping function. Heart represents an anatomical pump that, with its contractions maintains a balance between cardiac output and venous return. It is located in the thoracic cavity, behind and to the left of the breastbone, also called the sternum. Heart is divided into right and left halves, and each half is subdivided into two chambers: upper chambers,

called atria, are separated by a muscular partition known as the interatrial septum; lower chambers, the ventricles, are separated by the interventricular septum.

Two main circulatory loops compose the cardiovascular system: the *pulmonary circulation loop*, the smaller one, transporting deoxygenated blood from the right side of the heart to the lungs, where blood is oxygenated and returns to the left side of the heart; the *systemic circulation loop*, the larger one, carrying highly oxygenated blood from the left side of the heart to all body's tissues, removing metabolic wastes and returning deoxygenated blood to the right side of the heart. A representative scheme of cardiovascular system is provided by figure 1.1.

Pulmonary circulation starts from the right ventricle of the heart, where the blood is pumped into the pulmonary arteries and into the lungs; once the exchange of gases between the capillaries and the alveoli has occurred, the oxygenated blood flows through the pulmonary veins and back into the left atrium of the heart. Through the mitral valve, blood fills the left ventricle. Heart's pumping action forces the blood through the aortic valve and to all parts of the body reached by systemic circulation. In its passage through capillaries of the body blood gives up to the tissues the

materials necessary for their growth and nourishment, and at the same time receives from the tissues the waste products resulting from their metabolism (Gray, 1918).

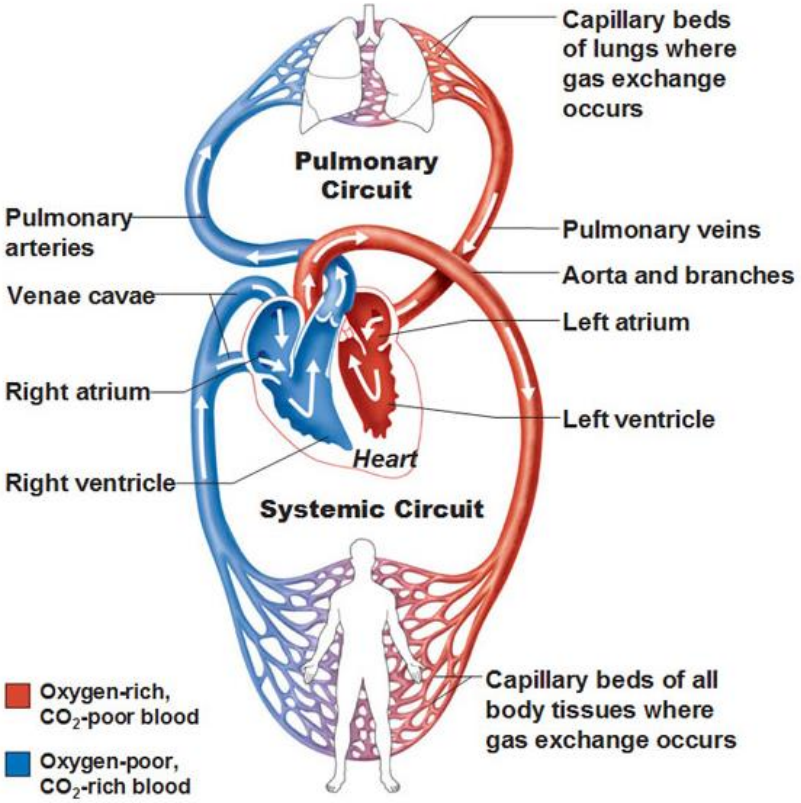

Figure 1.1 Scheme of human cardiovascular system. Heart, pulmonary and systemic circulation loops are sketched (from *www.pixgood.com*).

Deoxygenated blood flows into the collecting veins that all end up merging into either the superior vena cava, which collects blood from head, neck, thorax and upper limbs or the inferior vena cava, which receives blood from abdomen and lower limbs. Both the superior and inferior vena cava drain blood into the right atrium. Flowing through the tricuspid valve, blood fills the right ventricle where the process starts all over again with the pulmonary circulation (Figure 1.1).

Blood is a fluid connective tissue. It consists of a cellular suspension in a complex solution, named plasma. Cells constituting blood suspension are erythrocytes (or red blood cells), leukocytes (or white blood cells) and platelets. Water, proteins, lipids, inorganic salts, carbohydrates and derived ions compose the plasma.

Red blood cells are small semisolid particles with an average diameter of $7.5 \cdot 10^{-3}$ mm and an average density equal to 1.098 g/cm^3 (Schneck, 1995), increasing blood viscosity and affecting fluid behaviour (Ku, 1997). Typically comprising approximately, the 40% of blood by volume, erythrocytes carry respiratory gases through cardiovascular system. Leukocytes are cells of the immune system, with a mean diameter ranging between $6 \cdot 10^{-3}$ mm and $10 \cdot 10^{-3}$ mm and a mean density between 1.055 and 1.085 g/cm^3. White

blood cells defend the body against both infectious disease and foreign materials. Platelets are the smaller cellular blood components with average diameter and density equal to $3 \cdot 10^{-3}$ mm and 1.085 g/cm^3, respectively (Schneck, 1995). Platelets have an irregular shape and are anucleate cells involved in hemostasis, leading to the formation of blood clots.

Blood perfuses all the body and exchanges material (oxygen, nutritive materials, hormones, carbon dioxide, metabolic products) with the body tissues. It also provides for maintaining a stable body temperature and pH in order to keep homeostatic conditions.

Blood is transported through the whole body by a continuum of vessels. Blood vessels are the body's highways allowing blood to quickly and efficiently flow from the heart to every region of the body and back again.

The size of blood vessels decreases from the heart to the periphery of the body, with the reduction of the characterizing pressures range, in order to access all the peripheral areas. All vessels are characterized by a hollow area called lumen through which blood is able to flow. Blood vessels are divided in three main types: arteries (with a sub-distinction in large, mean and small arteries), capillaries and veins (smaller veins

are called venules). A representative sketch of the human vascular network is provided by figure 1.2.

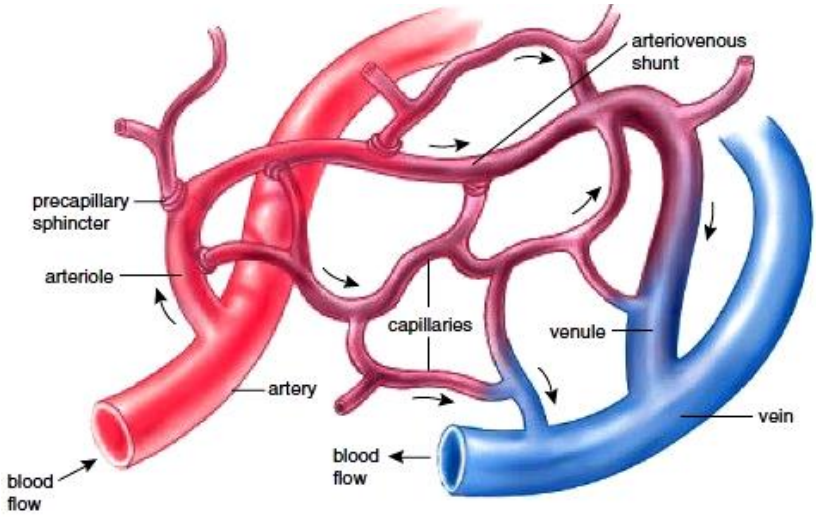

Figure 1.2 Scheme of human vascular network depicting differences among arteries, arterioles, capillaries, venules and veins.

Arteries usually carry highly oxygenated blood away from the heart, with the exception of arteries of the pulmonary circulation loop which carry blood poor in oxygen from the heart to the lungs to be oxygenated. Arteries, carrying blood being pushed from the heart, are subjected to high blood pressure levels (typically, 80-120 mmHg). In order to face this pressure, arterial wall is thicker, more elastic, and more

muscular than those of other vessels. Largest arteries of the body contain higher percentages of elastic tissue allowing them to stretch, accommodating the peak of blood pressure waveform. Instead, smaller arteries have a more muscular structure of the wall: smooth muscles of their wall contract or expand to regulating blood flowing through their lumen.

Arterioles are smaller arteries branching off from larger arteries and carrying blood to capillaries. Characterized by much lower blood pressures (than bigger arteries), decreased blood volume because of their big number, arterioles have walls much thinner than those of arteries.

Capillaries are the smallest and thinnest blood vessels in composing cardiovascular system. Connecting arterioles to venules, these vessels carry blood very close to the tissues' cells in order to very efficiently exchange gases, nutrients, and waste products. The wall of capillaries consists of only a thin layer of endothelial cells (endothelium) placing the minimum amount of structure possible between blood and tissues. The endothelium acts as a porous membrane allowing liquids, dissolved gases, and other chemicals to diffuse along their concentration gradients into or out of tissues.

Veins are the large return vessels of the body, acting as the blood return counterparts of arteries. Because the arterial

vessels absorb most of the force of the heart's contractions smoothing blood pressure waveform, veins and venules are subjected to very low pressure' levels. For this reason, the wall of veins is much thinner, less elastic, and less muscular than arterial wall. In order to avoid inverse flow and to facilitate counter-gravity blood flowing, veins could contain one-way valves.

Venules are smaller venous vessels connecting capillaries to veins; they collect deoxygenated blood from capillaries into larger veins for back flow to the heart.

1.2.2 Histology of arterial blood vessels

Blood flow and pressure waveforms are time-dependent. The heart ejects and fills with blood in alternating cycles called systole and diastole: blood leaves the heart during systole, and rests during diastole, when no blood is ejected. Heart pumping action creates pulsatile conditions in all arteries, which have to expand to accept the blood being forced into them from the heart, and then squeeze this blood on to the veins when the heart relaxes.

Arteries are biologically active organs that maintain their own integrity and homeostasis through mechanism regulated within the vessel wall. Figure 1.3 shows the typical structure

of the wall of an arterial blood vessel, composed of endothelial cells, smooth muscle cells and extracellular matrix, including collagen and elastin. These vascular wall components are arranged into three concentric layers called tunica *intima*, *media* and *adventitia*.

The tunica intima is the thinnest and innermost layer. It is composed of a single layer of endothelial cells and a small amount of subendothelial connective tissue. The intima is the only barrier between blood and its components and the thrombogenic tissues understanding. The endothelial cells are in direct contact with the blood flow and act as a lining inside the arteries, both providing an antithrombogenic surface regulating the transport of macromolecules from the blood into the outer layers of the vessel wall. A dense elastic membrane called *internal elastic lamina* separates the tunica media from the tunica media; it is composed of elastic fibers scattered and arranged in longitudinal direction. This membrane is discontinuous and through its holes some muscle cells could penetrate the tunica intima.

The tunica media, composed of multiple layers of smooth muscle cells, elastic fibers and connective tissue, is the thickest layer of the vessel wall. It provides structural support, vasoreactivity and elasticity. The tunica media is responsible

for the compliance of the artery during cardiac cycle, accumulating and releasing energy in response to blood pressure variations. The amount of different components of the tunica media varies depending on the type of arterial vessel. Smooth muscle cells contraction and relaxation (resulting in vasoconstriction and vasorelaxation, respectively) are regulated by autonomic nerves (*nervi vasorum*) and local metabolic species. Vessel expansion and contraction, respectively with systole and diastole, are allowed by elastic fibers. The media is separated from the adventitia by a dense elastic membrane called the *external elastic lamina*.

The tunica adventitia, composed of connective tissue as well as collagen and elastic fibers, nutrient vessels (*vasa vasorum*) and autonomic nerves, is the outermost layer the outer layer of vascular wall. In particular, the collagen serves to anchor the blood vessel to nearby organs and the elastic fibers, arranged as a counter-rotating helical system, allow the arteries to stretch and protect the vessel in case of large deformations.

As arteries become smaller, wall thickness gradually decreases. Capillaries consist only of a single layer of

endothelial cells on a basement membrane. There is no media or adventitia.

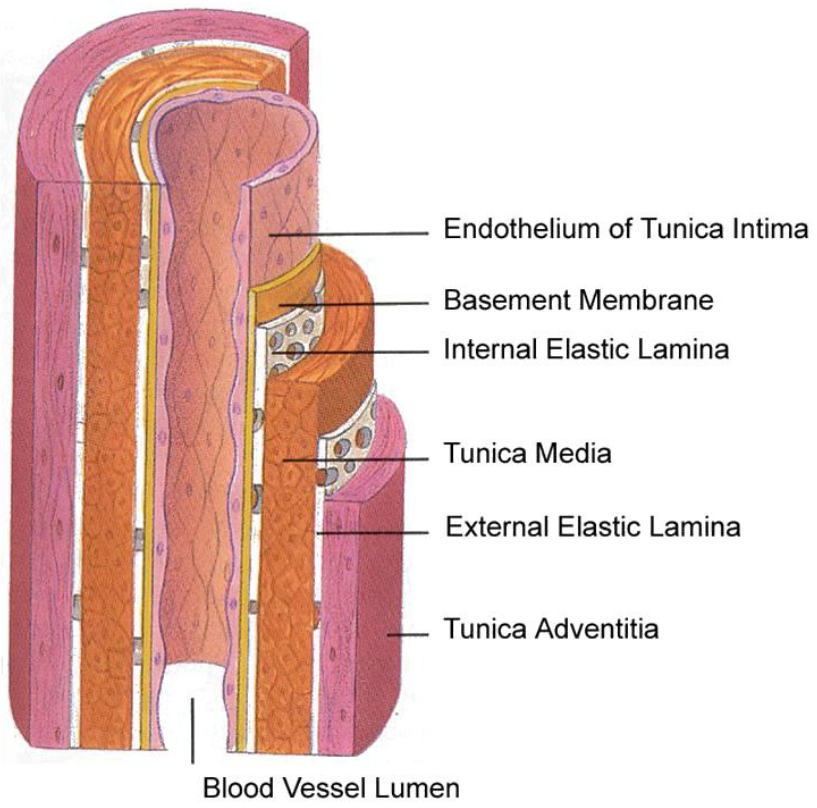

Figure 1.3 Schematic of arterial wall structure.

1.2.3 The Aorta

The cardiovascular district considered in this thesis is the thoracic aorta. The aorta is the largest blood vessel of the systemic circulation and it represents the main trunk of the cardiovascular system delivering the oxygenate blood to the whole body. All the arteries, except for the pulmonary arteries, originate from the aorta or its branches and carry blood towards all the organs and the other structures of the body for their nutrition (Gray, 1918).

The aorta can be divided in several portions as shown in figure 1.4. The aortic vessel arises at the left ventricle of the heart, from which it is separated by the aortic valve, with a diameter of about 3 cm. It moves upward for a short distance forming the so called ascending aorta (AAo). After ascending, the aorta bends backward, giving rise to the aortic arch, and starts descending through the diaphragm; the descending portion is called descending aorta (DAo). It ends at the height of the fourth lumbar vertebra, by dividing into the right and left common iliac arteries. The AAo is the first short part of the aorta, with a length of about 5 cm. It begins in the line of pericardium, rising from the left ventricle. The ascending aorta describes a slight curve in its course, passing obliquely upward, forward, and to the right, with respect to the direction

of the heart's axis. Above its origin it presents the three aortic sinuses of Valsalva, after which there is a bulge called aortic bulb. Another expansion is the large aortic sinus. From the base of the aorta originate the only branches of the ascending aorta, the left and right coronary arteries, that supply heart with blood.

The second portion of the aorta is the aortic arc, a banded path linking the ascending to the descending part of the aortic vessel. From the aortic arc originate three main vessels, as shown in figure 1.4: the common trunk (or innominate artery or brachiocephalic artery, BCA), the left common carotid artery (LCCA) and the left subclavian artery (LSA). These three large supra-aortic vessels are designed to supply head, neck and arms with oxygenated blood. The BCA, in particular, divides in two ramifications, the right subclavian artery and the right common carotid artery.

The third and last portion of the aorta is the descending aorta. It gets this name because it runs down, descending through the diaphragm. It is further divided in two main parts: the thoracic aorta, descending within the thorax on the left side of the sternum, and the abdominal aorta, ending by dividing into the right and left common iliac arteries.

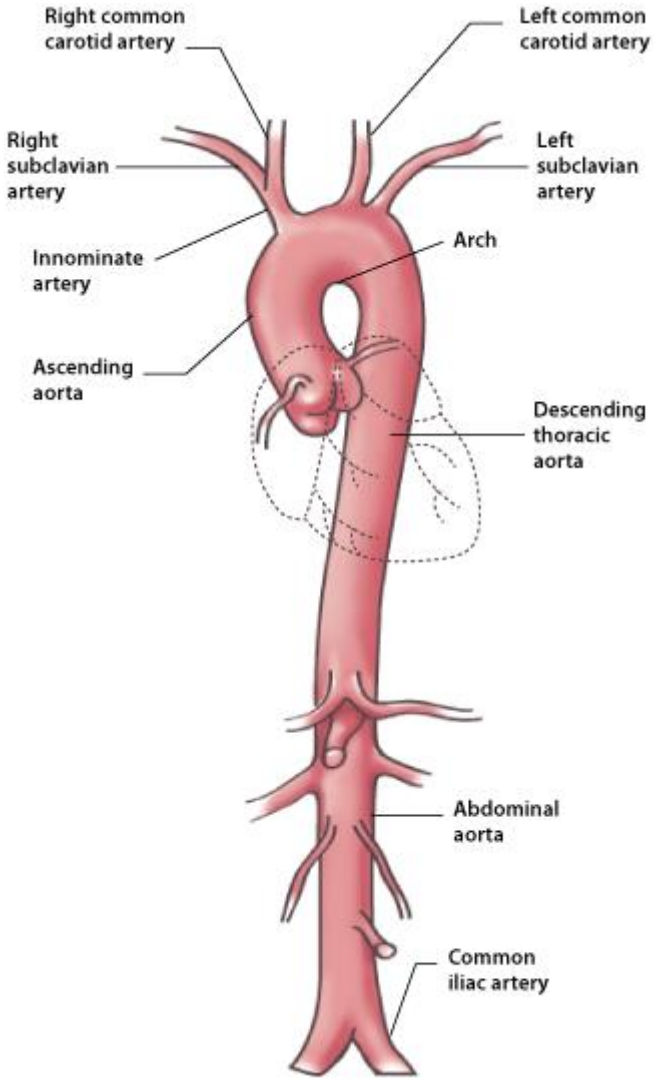

Figure 1.4 Schematic of the largest artery of the human body: the aorta. The main aortic portions and branches are indicated.

Eventually the aorta ends, with a much more reduced diameter of about 1.75 cm. The thoracic aorta indeed has a complex geometry characterized by twisting, branching, taper and non-planar curvature.

1.3 Atherosclerosis

Atherosclerosis is a specific form of arteriosclerosis, the generic term for a group of pathological states characterized by the hardening, thickening and loss of elasticity of arterial walls. It is a major cause of death in developed countries.

Although atherosclerosis can affect any artery in the human body, it is usually located within large and medium arteries, especially the abdominal aorta, coronary arteries and the cerebral arteries. The characteristic element of atherosclerosis is the formation of plaques (called atheromas) within the arterial wall, consisting of a lipid core surrounded by an external fibrous capsule, and a series of different cellular types such as macrophage cells, platelets and fibroblasts. These atheromatic plaques gradually narrow the lumen and become the site of bleeding and thrombus formation, that can eventually lead to myocardial infarction or stroke.

1.3.1 Epidemiology of Atherosclerosis

The etiological factors of atherosclerosis have not yet been fully elucidated. It is very likely that the genesis of atherosclerosis is multifactorial; the disease would depend on a group of factors that are related to one another. Several well-identified risk factors (i.e., hypertension, hyperlipidemia, diabetes mellitus, obesity, and cigarette smoking) are implicated in its pathogenesis. The disease tends to be gradual, often taking decades before the affected person is in danger of cardiovascular or cerebrovascular problems.

The development of atherosclerosis is complicated (a schematic example is provided by figure 1.5). For years, two have been the most accredited pathogenetic hypothesis of atherosclerosis: the lipid hypothesis and the endothelial damage hypothesis.

According to the lipid hypothesis, patients with high serum cholesterol concentrations have a higher incidence of atherosclerosis, and since 70% of this cholesterol is transported in low-density lipoproteins (LDL), the development of atherosclerosis correlates closely with increased LDL levels (Nielsen, 1996). LDL seems to be more prone to pass through the endothelial cells' monolayer, reaching the innermost layer of the artery (the intima). As the

fat deposits become larger, inflammatory white blood cells, called macrophages, gather at the site of the lipid deposition trying to remove it from the wall of the artery. Once monocytes traverse the endothelium, they become engorged with oxidized lipids forming foam cells, which grow increasingly inefficient at lipid removal and undergo cell death, accumulating at the site of lipid deposition. As these focal lipid deposits grow larger, they become atherosclerotic plaques protruding into the lumen of the artery and producing lumen narrowing (as shown in figure 1.7). The main limitation of this first hypothesis is that it does not explain smooth muscle cells proliferation.

The second hypothesis considers the chronic endothelial damage as the primary event in the pathogenesis of atherosclerosis and the reaction to it may eventually lead to plaque formation. This hypothesis suggests that blood flow and other mechanisms in the long run cause a loss of endothelium recalling that adhering and aggregating platelets release substances that stimulate the migration of smooth muscle cells from the tunica media to the intima; these muscle cells replicate synthesizing connective tissue and proteoglycans to form a fibrous plaque. Also in this case, the

hypothesis presents a problem related to the fact that endothelium remains intact.

In order to overcome these limitations, the two hypotheses converged in the unifying one. This theory is based on the fact that the primary event of atherosclerosis development seems to be repeated and subtle injury (including alteration in cell ligand expression, increased wall permeability and endothelial turnover) to the artery's wall thought various mechanisms. These mechanisms include physical stresses exerted by blood flow, and inflammatory stresses involving the immune system, certain infection, or chemical abnormalities in the bloodstream (high cholesterol, diabetes). The damage of the arterial endothelium causes adhesion molecules production by cells, promoting monocytes rolling, adhesion and migration into the intima. Here, as described, monocytes form foam cells, engulfing oxidized lipids (Figure 1.5) and provoking an inflammatory immune response that causes further damage to the artery wall. This, over time, lead to an even more serious damage of the endothelial layer, allowing and promoting the penetration into the arterial wall of toxic LDL cholesterol molecules.

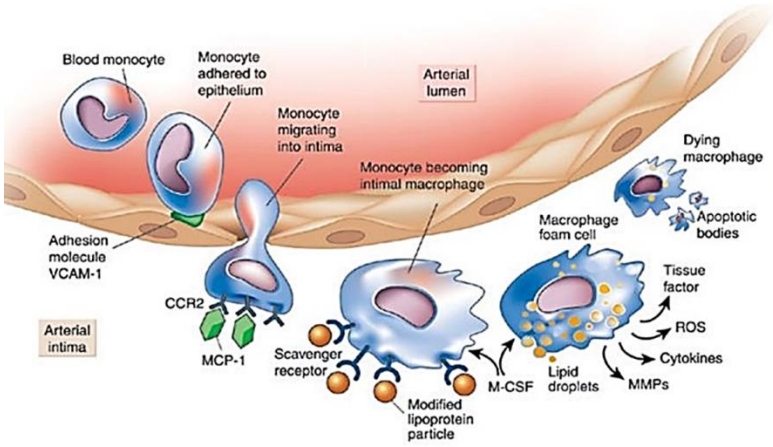

Figure 1.5 Schematic of the blood-vessel interaction leading to atherosclerosis.

Low-density lipoproteins, after penetrating the vessel wall, are exposed to free radicals, which are products of the immune response. This lead to the oxidation of LDL molecules and, so, to the formation of oxidized LDL, which release toxins into the vessel wall aggravating the injury and causing the recruiting of a higher number of monocytes from the blood flow. This results in an exacerbation of wall injury, allowing more LDL penetration into the vessel wall. These components gradually form a lipid foam, constituting the early stage of the atherosclerotic plaque. The plaque slowly protrudes in the vascular lumen, with no symptoms for the subject. Its exposition to circulating blood promotes minerals, such as

calcium, deposition, covering the plaque with a hard shell. Basing on their components, atherosclerotic plaques may range from a soft fatty plaque to a hard one rich in collagen.

1.3.2 Low-density lipoproteins

Low-density lipoproteins are one of the five main groups of lipoproteins. In particular, LDL are specialized in lipid transport and transfer around the body, through the circulatory system. A predominance of small dense LDL particles is associated with an increased risk of coronary disease (Musliner and Krauss, 1988). This is the reason why LDL is better known as “bad cholesterol” (even if, it is actually the lipoprotein form, and not the cholesterol carried by the particle, that is related to cardiovascular disease risk).

Lipoproteins are submicroscopic particles with a hydrophobic lipid core surrounded by a monolayer of proteins and amphipathic lipids. In particular, the lipids carried by the low-density lipoproteins are predominately cholesteryl esters, cholesterol and triglycerides, and the proteic component is formed of one single copy of an apolipoprotein molecule, called Apolipoprotein B100 (Apo-B100), and some additional ancillary proteins. Figure 1.6 shows the general structure of a LDL particle.

The specific composition of LDL, in particular its proteic component, determines the density of the whole complex. LDL particles, for example, are characterized by a density ranging between 1.019 g/ml and 1.063 g/ml and an average diameter of 22 nm. Since there are different types of LDL particles with a variable number of fatty molecules, usually, a distribution of mass and size of LDL particle could be observed in the blood flow. The determination of the overall structure of LDL particles is a very complex task, because of their highly heterogeneous and variable composition. Recently, the possible relationship between structure and function of native LDL particles at physiological body temperature has been investigated, through three-dimensional cryoEM reconstruction (Kumar et al., 2011).

The main role of low-density lipoproteins is to deliver mainly esterified and unesterified cholesterol to the peripheral tissues through the blood, thanks to the amphiphilic nature of its shell. In order to maintain the concentration of circulating LDL at a physiological level, specific receptors, situated mainly in the liver, remove the particles from the circulation by breaking them down. Once the needed quantity of cholesterol has been delivered to the cell, the cell itself interrupts the LDL receptor synthesis, preventing the

increasing of intracellular cholesterol concentration (Brown and Goldstein, 1986).

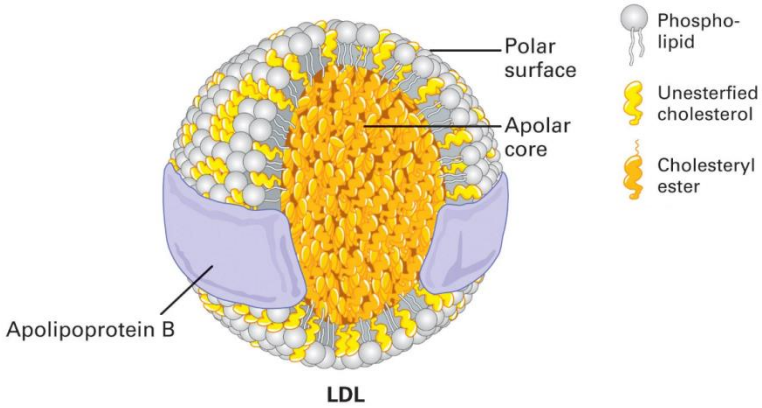

Figure 1.6 Schematic of a LDL complex (from *www.healthyprotocols.com*).

1.3.3 The role of low-density lipoproteins in atherosclerosis

As previously stated, atherosclerosis is a cardiovascular disease characterized by chronic inflammation of a damaged intima. Even if the atherosclerotic process is still not fully understood, it is well accepted that an abnormally high accumulation of macromolecules, such as LDLs, within the arterial wall is a typical characteristic of the early

atherogenesis. In particular, it is thought that the retention of LDL particles, together with the inflammation, leads to the endothelial cell dysfunction that starts the atherosclerotic process. However, it is not clear if this retention of LDL particles near the wall represents a cause or a consequence of atherogenesis (Zang et al., 2008).

Atherosclerosis is the result of an extremely long process and its symptoms are not immediate; it starts with inflammatory processes that set off a cascade of responses over time and a study conducted by Napoli et al. (1997) demonstrates that early atherogenesis is prevalently found in human fetal aortas and that it is greatly enhanced by maternal hypercholesterolemia.

The pathological process starts with the accumulation of various LDL particles. In particular, small dense LDL particles seems to be more prone to reaching the intima. Inside the vessel wall, LDL particles are susceptible to oxidation by free radicals and endothelial cells respond to this inflammatory process by attracting monocytes from the bloodstream into the arterial wall, therefore transforming them into macrophages. Macrophages ingest oxidized LDL particles thus producing foam cells which, if are not able to process the oxidized LDL and recruiting high-density

lipoprotein (HDL) particles to remove the fats and cholesterol, they grow and, eventually, release fats, cellular membrane debris and oxidized materials in the artery wall, after their rupture.

The plaque formed at this stage will eventually become a complex atheroma. It will modify the mechanical properties of the wall by reducing its elasticity: the smooth muscle cells of the blood vessel, in fact, stretch in order to accommodate the growing plaque and the endothelial lining thickens. This, on one hand, contributes to compensate the narrowing of the lumen caused by the plaque but, on the other hand, it causes the artery wall to stiffen and become less compliant to stretching during each heartbeat, thus leading to an increased pressure within major arteries and an increased pumping work by the heart.

Previous studies have demonstrated that in order to become atherogenic, LDL particles have to be subjected to an oxidative modification (Steinberg et al., 1989; Brown and Goldstein, 1983). In detail, there are no doubts about the increasing risk for complications of atherosclerosis when cholesterol level in blood exceeds 160-180 mg/dl. However, it has been observed that the modification of LDL represents a prerequisite for macrophage uptake and cellular accumulation

of cholesterol. Several studies showed that: (1) monocytes and macrophages may not become foam cells even if exposed to high concentrations of native LDL (Brown and Goldstein, 1983; Golstein et al., 1979) and, so, (2) LDL molecules have to undergo certain post-secretory modification to be more rapidly taken up by macrophages, in order to convert them in foam cells (Steinberg et al., 1989). The LDL oxidative modification resulted to be mainly induced by endothelial cells (Henriksen et al., 1981), smooth-muscle cells (Henriksen et al., 1981; Heinecke et al., 1984), monocytes and macrophages (Morel et al., 1984). Hence, all three of the major cell types in the wall of arteries are able to induce a modification of LDL, affecting their atherogenic potential. For this reason, LDL oxidative modification seems to occur primarily in the tunica intima; significant degree of LDL oxidation cannot be observed in plasma because of its high antioxidant content (Witztum and Steinberg, 1991).

1.3.4 Hemodynamic factors in atherosclerosis

The pathogenesis of the atherosclerosis is modulated by several systemic and local factors, among which the blood properties, the vessel geometry, the mechanical properties of the vessel wall, and pressure gradients play an essential role.

Atherosclerotic lesions tend to develop in regions where blood flow is characterized by flow separation and reattachment, recirculation, stasis, jet-like flow and turbulence. This situation is often referred to with the expression “disturbed flow”, describing an atherogenic hemodynamic environment.

In literature it is widely documented the frequency of atherosclerosis occurrence at specific arterial districts and at vascular regions of curvature, bifurcation, sudden expansions and branching of the vessels. These combined observations confirm that local arterial hemodynamics and vessel geometry play a relevant role in promoting the onset and the development of the atherosclerotic plaque.

Among hemodynamics features, a key role is played by wall shear in preserving healthy physiological conditions. More in detail, WSS, representing the force per unit area exerted by flowing blood on the vascular wall, promotes the maintaining of the normal function of the cardiovascular system, encouraging endothelial cells adaptation to its long-term variations. Arterial vessels are able to change their conformation in order to re-establish physiological WSS: they dilate if subjected to increased WSS values, or the remodel to a smaller diameter in the presence of decreased WSS values

(Wootton and Ku, 1999). As concerns atherosclerotic disease, several studies have suggested that the persistent exposition of the vessel wall to low and oscillatory patterns of shear stress could lead to an intimal wall thickening (Caro et al., 1969; Friedman et al., 1981; Ku et al., 1985; Pedersen et al., 1997). Low and oscillatory values of WSS, usually indicating zone of blood stagnation, could encourage the interaction between the arterial wall and the various species transported by the flowing blood, increasing the particle residence time in the near-wall region and thus promoting atherogenic blood molecules uptake (Glagov et al., 1988; Shaaban and Duerinckx, 2000). Moreover, several in vivo and in vitro studies on endothelial cell conformation showed changes in cellular morphology if subjected to different flow conditions. In detail, it was observed that the endothelial cells exposed to laminar flows with a clearly definite direction (as in the straight arterial districts) tend to organize and orient themselves along the direction of the flow. On the contrary, cells subjected to not clearly directed flows, characterized by low and oscillatory values of shear stress, maintain a more polygonal conformation without a definite orientation, with a lack of the intercellular junctions organization and an increased wall permeability to atherogenic molecules

(Galbraith et al., 1998; Shaaban and Duerinchx, 2000). Figure 1.7 depicts changes in endothelial cells conformation and vulnerability to systemic apoptogenic stimuli, such as oxidized low-density lipoproteins. Cells of the endothelium if exposed to oscillatory slow blood flow may activate circulating monocytes and promote atherogenesis (Malek et al., 1999).

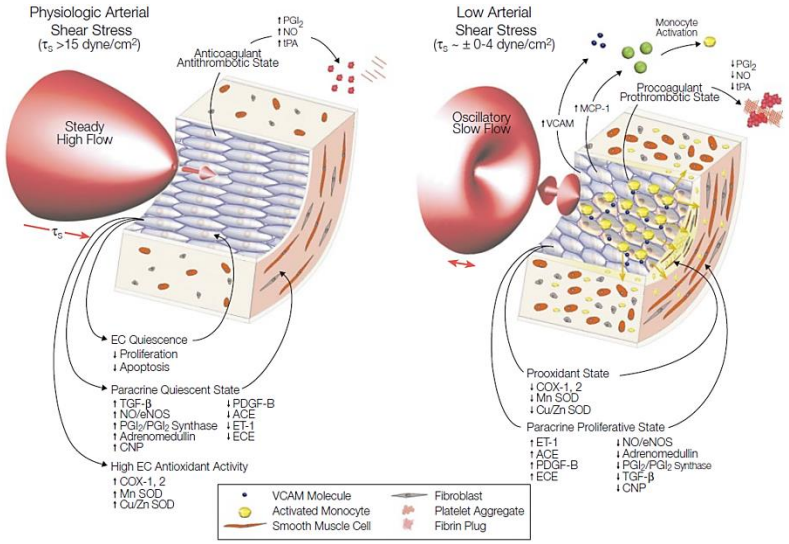

Figure 1.7 Illustration of the arterial endothelial phenotypic switch from ateroprotective (left panel) to atherogenic (right panel) induced by the local low and oscillatory pattern of shear stress (from Malek et al., 1999).

In order to quantitative assess the atherogenic risk of a specific vascular district, several descriptors have been proposed during years. In particular, concerning the near-wall hemodynamics, three are the widely accepted and "established" WSS-based descriptors: the time-averaged wall shear stress magnitude (TAWSS), oscillatory shear index (OSI), and relative residence time (RRT). These descriptors will be detailly explained in the Materials and Methods chapter of this book. In particular, TAWSS is useful to individuate luminal surface areas subjected to low values of WSS in average over the cardiac cycle; OSI highlights areas at the vessel wall characterized by higher oscillations in direction of the WSS vector over the cardiac cycle; RRT summarizes information given by TAWSS and OSI, indicating luminal surface areas exposed to both low and oscillatory WSS values overall the cardiac cycle.

1.3.5 Consequences of atherosclerosis

Atherosclerosis, with is consequences, represent one of the major causes of death in the industrialized countries.

The formation of the atherosclerotic plaque at the vascular wall and its protrusion in the vascular lumen may result in both occlusive and non-occlusive complications.

Occlusive complications of atherosclerosis consist mainly in chronic occlusive arterial diseases and occlusion by thrombus formation. In the first case, as the plaque grows in size, it tends to occlude the arterial vessel; this phenomenon is typical of the very large aortic branches, such as the carotid and iliac arteries, and it may occur very slowly over time starting with the narrowing of the lumen and leading to complete occlusion, as the disease progresses. In general, in case of chronic occlusion the vessel tends to adapt and remodel in order to maintain blood flow, therefore, chronic occlusion will not usually alter resting blood flow until lumen occlusion becomes greater than 70%; in this case resting blood flow is reduced and the patient is more likely to suffer from acute complications, such as myocardial infarction. On the other hand, vessel occlusion may also be caused by thrombus formation on the surface of the atherosclerotic plaque. In detail, under the effect of hemodynamic forces, the atheroma may ulcerate leading to immediate blood clotting at the site of the plaque rupture. In this case, since the thrombotic occlusion occurs very quickly, distal tissues will be damaged as a result of inadequate blood flow (ischemia). When ischemia occurs in the coronary circulation, the occlusion results in a

myocardial infarction; when it occurs in the cerebral circulation, the result is stroke.

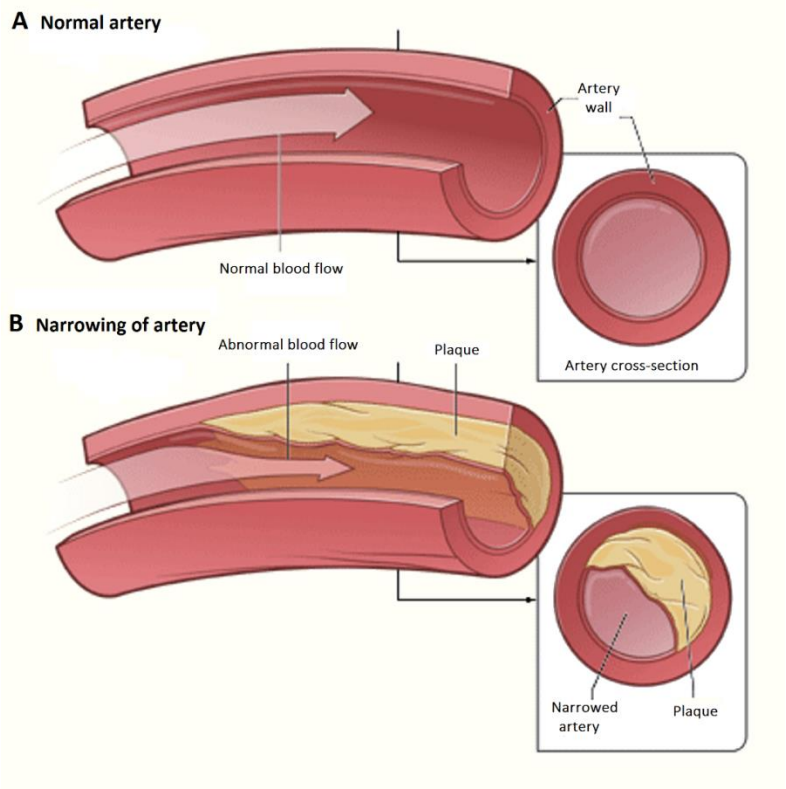

Figure 1.8 A) A normal artery with a normal blood flow. B) An artery with atherosclerotic plaque and abnormal blood flow. (from *www.nhlbi.nih.gov/health*).

Non-occlusive complications, on the contrary, are caused by changes in the mechanical properties and stability of the artery. For example, the aorta and the iliac arteries, when sclerotic, sometimes weaken becoming mechanically unstable and dilated, forming aneurysms. The aneurysms may lead to the formation of blood clots or they may rupture and hemorrhage. The aorta also loses its elasticity and may calcify: this hardening translates into an elevated flow resistance encountered by the blood ejected from the left ventricle, thus increasing the cardiac work and the systolic blood pressure. These factors may then be important in the development of heart failure and high blood pressure.

A schematic example of a non-occlusive atherosclerotic plaque is provided by figure 1.7, displaying the differences between a normal artery and an arterial vessel narrowed by atherosclerotic plaque formation.

1.4 Overview of proposed computational model for LDL transport in Aorta

During last decade the interest of Scientific Community in computational fluid dynamics (CFD) models as promising tools to describe, analyze or predict the occurrence and progression of human diseases has risen. In particular, CFD

has supported the comprehension of hemodynamics flow patterns characterizing the aortic arch, providing highly resolved blood flow features in realistic arterial models. Starting from patient-specific anatomical and hemodynamic information given by PC-MRI, fully personalized flow simulation could be implemented, leading to a subject-specific oriented approach of disease computational investigation (Morbiducci et al, 2013).

In this contest, CFD has been seen as a powerful way to analyze the impact of specific haemodynamic flow patterns on mass transport in arteries. Personalized modeling of LDL transfer has been proposed to highlight possible atherogenic abnormalities in mass transfer. The use of a numerical approach to mass transport problem in arterial districts, indeed, should be often preferred with respect to *in vivo*, *ex vivo* or *in vitro* experimentations mainly for the possible high resolution of obtained data and the relative ease of conducting parametric studies (Ethier, 2002). However, CFD models require some assumptions which reflect on simulation results.

Several studies have been conducted on simulating LDL transport and transfer to wall in arterial districts, and, in particular, in thoracic aorta. Focusing the attention on last decades (2011-2017), some works have been published to

show and highlight the impact of selected assumptions, about problem formulation and fluid properties, on numerical simulations of mass transport in aorta.

In "*Effect of non-Newtonian and pulsatile blood flow on mass transport in the human aorta*" Liu et al. described the effect of non-Newtonian (Carreau model) pulsatile blood flow on LDL transfer to the wall of a subject-specific model of human aorta. Results from this study showed that both the assumptions have an impact on LDL polarization, significantly affecting luminal regions characterized by higher level of LDL concentrations. More in detail, assuming a non-Newtonian blood behavior reflects on higher LDL polarization; on the contrary, the pulsation of blood flow lead to a remarkably decrease of LDL concentration (Liu et al., 2011). Five years later, Soulis and colleagues extended the analysis to three more non-Newtonian fluid behaviors. They concluded that the assumption of non-Newtonian Power Law model for blood gives the most satisfying results. Moreover, obtained results highlighted a strong correlation between relative residence time (RRT) and LDL polarization (Soulis et al., 2016).

A comparison between the application of laminar or turbulence (Large Eddy Simulation) model, in terms of

resulting LDL distribution at the wall of a personalized aortic model, was made by Lantz and Karlsson. The unsteady-state analysis showed that the obtained small temporal changes of LDL luminal concentration during cardiac cycle when flow was treated as laminar, were significantly affected by the choice of a turbulence model. In region with disturbed flow, LDL polarization revealed to be sensitive to not only WSS but also near-wall flow (Lantz and Karlsson, 2012).

Several other papers highlighted the possible insufficiency of WSS magnitude alone to correct predict the luminal locations with higher LDL uptake (Soulis et al., 2014, 2016; Lei et al., 2015; Alimohammadi et al., 2016, 2017). These works pointed out the needing of a well refined near-wall model meshing, with the accurate definition of a boundary layer, because of the relevant role of near-wall hemodynamics in determining high LDL concentration at the vessel wall. Moreover, Alimohammadi and colleagues proposed a new index able to efficiently locate luminal areas of LDL polarization. As for RRT, it emphasizes both oscillatory and low magnitude WSS.

LDL transport and wall transfer depend on hemodynamic flow patterns developing in the analyzing vascular district, and so, on the specific vessel geometry. Lei et al. (2015)

investigated the influence of model geometry on LDL transport and polarization in a specific case of virtual intervention. Results from steady-state simulations showed that the presence of a fusiform aneurysm along the thoracic aorta promote a higher LDL uptake at the vascular wall. Chen et al. (2014) also analyzed the impact of geometry on mass transport. Results of the numerical investigation in three personalized models of deformed aorta showed that curvature and stenosis have marked effects on blood flow and on mass transport.

Recently researchers started to investigate the role played by other fluid-dynamic quantities in LDL transport through arterial wall. Mpairaktaris and colleagues, in particular, found that LDL transport and wall distribution are markedly affected by transmural pressure. By conducting steady-state simulations on a patient-specific model of thoracic aorta, indeed, they identified a correlation between elevated transmural pressure and LDL polarization (Mpairaktaris et al., 2017).

Although all analyzed complications characterizing the proper case construction for simulating LDL transport and wall transfer in personalized models of human aorta, none has focused the attention on boundary and initial conditions

definition. In studies presented in this paragraph, indeed, several fluid-dynamic inflow boundary conditions have been applied. In detail, steady-state simulations have been conducted by imposing a flat (Liu et al., 2011; Chen et al., 2014; Soulis et al., 2014; Lei et al., 2015) or a parabolic (Mpairaktaris et al., 2017) inflow velocity profile; unsteady-state simulations have been conducted by applying a pulsatile flat velocity profile (Liu et al., 2011; Alimohammadi et al., 2016, 2017; Soulis et al., 2016). No clear information about the imposed inflow velocity profile for the conducted unsteady-state simulations has been provided by Lantz and Karlsson (2012).

As regards mass transport problem, even if applied boundary conditions are quite the same, with few differences in equation describing LDL diffusion across the model wall (i.e. by advection-diffusion equation or permeability model), the imposed initial condition for LDL distribution is not declared.

1.5 Aim of the thesis project

Circumstantial evidence suggests a key role for mass transport in atherogenesis, with the accumulation process of high molecular weight solutes in the arterial intima considered

as a hallmark of early atherosclerosis (Caro et al., 1971; Getz, 1990; Stary et al., 1994). In particular, it has been observed that high plasma levels of low-density lipoproteins (LDL) are causally related to the development of atherosclerotic lesions (Nielsen, 1996). Low-density lipoproteins are the most abundant atherogenic lipoproteins in flowing blood (Tarbell, 2003). The LDL transfer from flowing blood to the arterial wall has been proposed to be mainly consequence of a convective transport rate process (promoted by an arterial pressure-driven transmural flux of water in the lumen-to-wall direction), that ultimately results in a LDL concentration polarization at the surface of the endothelial barrier (Deng et al., 1993; Deng et al., 1995; Lever et al., 1992; Wada and Karino, 1999). This boundary layer, giving rise to near-wall local elevated LDL concentrations, promotes LDL transfer into the arterial wall in disturbed shear regions (see, e.g., Ethier, 2002; Sill et al. 1995; Sun et al. 2006; Wada and Karino, 2002; and references therein).

However, (1) the general picture that regions at the lumen with elevated LDL polarization tend to co-localize with regions where atherosclerotic lesions develop, and (2) the observed tendency of such regions to co-localize with atherogenic wall shear stress (WSS) phenotypes, suggest but

do not definitively prove that blood-to-wall LDL transfer is a primary factor promoting atherogenesis (Ethier, 2002). The fact that mass transfer to the arterial wall is regulated by complex and nonlinear mechanisms (Tarbell, 2003; Vincent and Weinberg, 2014), including WSS-related effects (Kang et al., 2014), markedly contributes to complicate the picture.

Advanced computational fluid dynamics coupled with medical imaging allows to combine the anatomical and hemodynamic inputs to realistic, fully personalized flow simulations to study local hemodynamics in arteries. Such an approach represents an effective way when addressing the still open questions about the role of blood-side LDL transfer to the arterial wall in atherogenesis (Ethier, 2002). In particular, personalized computational models have been proposed to study LDL blood-to-wall transfer in the aorta (Alimohammadi et al., 2016; Chen et al., 2014; Lantz and Karlsson, 2012; Lei et al., 2015; Li et al., 2017; Liu et al., 2009; Liu et al., 2011; Soulis et al., 2016), a district of election for the study of the relationships between the intricate local hemodynamics (Kilner et al., 1993; Morbiducci et al., 2011), LDL transport and disease.

However, computational hemodynamics requires some assumptions that could affect the solutions of the equations

governing blood flow and the aortic convective LDL transport. In previous studies of my research group, it has been demonstrated that different strategies in applying boundary conditions (BCs) derived from phase-contrast MRI (PC-MRI) measurements could lead to different results in terms of distribution of near-wall and intravascular flow quantities (Gallo et al., 2012; Morbiducci et al., 2013). In particular, it has been reported that idealized velocity profiles as aortic inflow BCs could not be sufficiently representative of the aortic hemodynamics (Morbiducci et al., 2013). Additionally, a paucity of data characterizes the literature concerning the BCs and initial conditions adopted to model LDL transport. In most recent studies focused on LDL transport in image-based aortic geometries, indeed, the choice of the imposed initialization for LDL concentration is scarcely documented, as discussed in the previous paragraph.

The aim of this study is to analyze the impact that different possible strategies of applying (1) PC-MRI measured data as inflow BC, and (2) LDL concentration profiles as IC, have on LDL blood-to-wall transfer modelling in the human aorta.

Here for the first time the problem of the unavailability of in vivo data to properly set concentration profile ICs in

computational modelling of LDL transfer in aorta is faced up. The impact of applied BC-IC strategies on LDL blood-to-wall transfer is evaluated in terms of computational costs and LDL polarization profiles at the luminal surface. Moreover, by virtue of the reported high LDL concentration in correspondence of disturbed shear regions (Ethier, 2002; Sill et al., 1995; Sun et al., 2006), here a co-localization analysis with areas exposed to atheroprone WSS phenotype is proposed as a "physics consistency check".

The study here presented would contribute to clarify which is (1) the level of detail obtained from measured flow data to be used as inflow BC, and (2) the plausibility of hypotheses on LDL concentration to be used as IC strategy, to satisfactorily simulate mass transport/transfer in personalized computational hemodynamic models of human aorta.

Chapter 2

Materials and Methods

This chapter focuses on the methods of the study providing a detailed overview of the steps followed to reconstruct the model, generate the mesh and conduct the simulation on the investigating anatomical domain, starting from acquired clinical images and measured velocity and flowrate data.

The workflow of the followed from- in vivo- to- in silico approach is depicted in figure 2.1. More in detail, the upper part of the blocks-diagram concerns the image-based model reconstruction process and the definition of velocity and flowrate profiles, over the cardiac cycle, starting from in vivo

measured data. The lower part refers to the construction of the case of simulation, with the definition of the solver, the material properties, the convergence criteria and with the imposition of boundary and initial conditions for the simulations.

The workflow is completed by blocks titled as “Results”, for both steady-state and unsteady state simulations. In particular, “Results” block of unsteady-state simulations summarizes the followed methods of simulation results analysis. It lists the simulation resulting variables on which the post-processing analysis is focused.

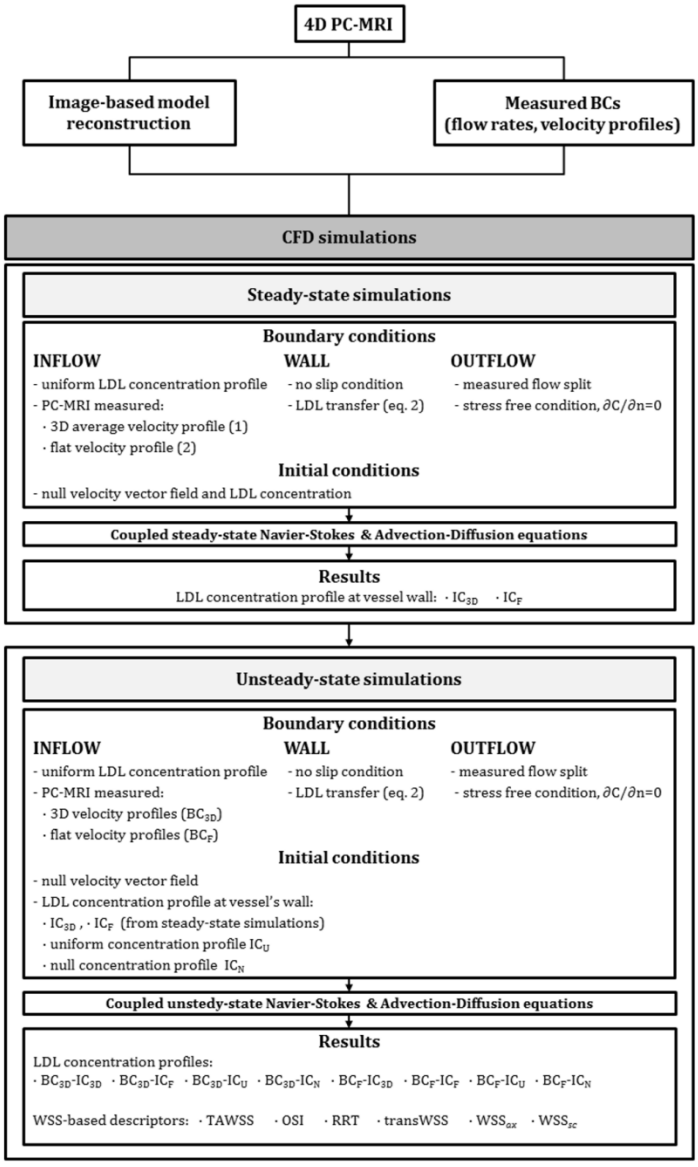

Figure 2.1 Scheme of the methodology applied to investigate the impact that the applied BC-IC strategy has on blood-side LDL transfer to the aortic wall

2.1 Computational Model

2.1.1 Image-based model reconstruction

The anatomical model of an ostensibly healthy human aorta was reconstructed starting from four-dimensional Phase Contrast Magnetic Resonance Imaging (4D PC MRI) images acquired using a 1.5 Tesla scanner (Achieva, Philips Healthcare, The Netherlands). Anatomical data and 3D blood velocity vector fields were acquired over twenty-two oblique sagittal slices, each one covering a field of view of 280 × 280 mm^2 and aligned with the aortic arch. The whole aorta was covered with an isotropic spatial sampling (measured voxel size = 2 × 2 mm^2; slice thickness = 4 mm, 2 mm slice spacing). A gradient echo spin sequence was used with velocity encoding (VENC) in all three directions, with the following set scan parameters: TR/TE = 5.4/3 ms; VENC=150 cm/s. In order to reduce motion artefact, a navigator echo technique was used. The phase-contrast pulse sequence was arranged to allow synchronization of the data to the cardiac cycle. This ensured to reconstruct a cine series of three-dimensional data sets from multiple phases of the cardiac cycle. The resulting cine pulse sequence was retrospectively gated to the electrocardiographic cycle

(cardiac rate of 54 bpm) to obtain 22 cardiac phases (Gallo et al., 2012a; Morbiducci et al., 2009; Morbiducci et al., 2011; Volonghi et al., 2016).

PC-MRI slices were used to reconstruct the model of the investigated aorta into the Vascular Modeling Toolkit (VMTK) environment (an open source software, available to be downloaded at http://www.vmtk.org/). The applied approach for the extraction of the surface mesh of the aorta from PC-MRI data consisted of two steps: (1) the creation of an image representing the velocity modulus and (2) the obtaining of the mesh representation of the investigating anatomical domain, starting from this new image. In detail, the first step regarded the creation of an additional image containing the velocity modulus starting from the three acquired gray-scale images, displaying the three velocity vector components, by calculating the magnitude of the velocity vector.

As concerns the second one, a multiple step VMTK procedure was applied for the extraction of the polygonal surface mesh of the thoracic aorta and for the creation of an accurate vessel volume from the new image, as detailed described in Gallo et al., 2012a and Morbiducci et al. 2013. Therefore, the image representing the velocity modulus was

segmented into a level set representation, using an implicit deformable models algorithm (Antiga et al., 2008). In detail, in a level set representation the surface of interest represents the zero level set of a three-dimensional function, usually called "level set function"; this function is used to represent the evolving contour of the deformable model. Moreover, using a deformable model, as the level set method, has the advantage that the location of the surface is independent of the chosen level, but instead it will locally conform to the peaks of the gradient modulus of the image levels, thus allowing for change of topology in a natural way. This means that the final surface will be located on the regions with the sharpest change of image intensity across the vessel wall.

The applied deformable models algorithm was initialized by providing a rough representation of the vessel geometry, obtained by the binarization of the gray-scale images representing the velocity modulus (obtained after the first step), by using a threshold value of 20 cm/s (corresponding to low values of vessel velocity during the systolic phase). In addition, five seed points were marked to define the vascular segments of interest. In detail, the first seed was positioned downstream of the aortic valve, identifying the inlet section of the ascending aorta (AAo); then four seeds were placed at the

other four sections delimiting the volume of the investigating vessel: at the end of the brachiocephalic artery (BCA), at the end of the left common carotid artery (LCCA), in the left subclavian artery (LSA) and at the end of the descending aorta (DAo). To create a more accurate vessel volume, the geodetic active contour algorithm was used (Antiga et al., 2008) and a marching cubes approach was adopted in order to create the polygonal surface mesh from this volume. Finally, to obtain the final smoothed surface mesh, a Taubin type non-shrinking filter was used as an additional step of shape regularization (Antiga et al., 2008; Gallo et al., 2012a). The obtained surface mesh was properly manually clipped at its delimiting surfaces with planes perpendicular to the vessel centerline in order to create distinctly defined surfaces for the accurate addiction to the final model of flow extensions and for the correct application of the boundary conditions. The model is displayed in figure 2.2.

Straight flow extensions were added to the outlet sections of the model (BCA, LCCA, LSA and DAo cross sections) in order to ensure a fully developed flow and to minimize the effect of outlet boundary conditions on the solution.

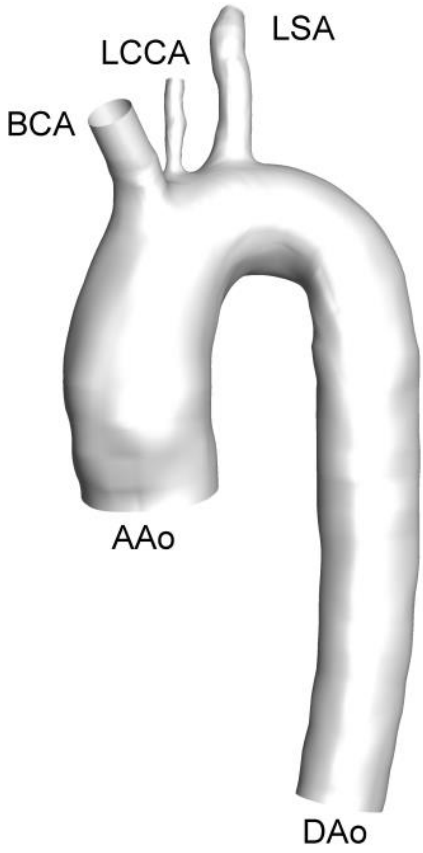

Figure 2.2 Resulting PC-MRI image-based model of the investigated thoracic aorta.

2.1.2 Model meshing

The finite volume method was adopted to solve coupled the governing equations of the fluid motion (the discretized

Navier-Stokes equations) and the advection-diffusion equations under unsteady flow conditions. In order to apply finite volume method, a computational mesh-grid of the investigated vascular domain was generated into the ICEM environment (ANSYS Inc., USA).

Since the problem governing equations are iteratively solved in each cell of the volume mesh generated from the geometric model, the mesh has to be appropriately computed in order to conduct to reliable results. In particular, it is important to assure the final outcome of the simulation to be independent of the number and size of mesh elements (cells). In fact, the number and distribution of the cells (i.e. mesh density) directly determine the accuracy of the numerical results and the computational cost. More in detail, meshes consisting in a higher number of elements, with smaller dimensions, and better defined in curvature, bifurcations or branching zones, allow to obtain more accurate results. However, more refined meshes require higher computational costs, needing of much more time to achieve the convergence results of the conducted simulation. For this reason, the choice of the final mesh, on which construct the simulation case, always plays a key role.

In this study, a mesh sensitivity analysis was carried out in order (1) to assure results independence of the built mesh and (2) to obtain a good compromise between solution accuracy and computational cost. More in detail, computational steady-state simulations of the investigating problem were performed by using the general purpose CFD code Fluent (ANSYS Inc., USA) on five computational grid of cardinality 4,300,000 in average. In particular, the impact of the boundary layer thickness and of the number of layers constituting the mesh near-wall region of prismatic cells was investigated, neglecting mean percentage errors in the order of 2-3% with respect to the mesh with the higher cardinality. Comparing simulation results in terms of WSS and LDL wall distribution, and so, identifying meshes assuring an acceptable accuracy, the one with the least number of elements, in order to reduce computational costs, was chosen as the final mesh.

The resulting mesh, generated into the ICEM environment, has a cardinality of 4,100,000. In detail, it consists of about $1.9 \cdot 10^6$ tetrahedral elements in the lumen region and 30 layers of high quality prismatic cells in the region near the model wall (boundary layer), as shown in figure 2.3.

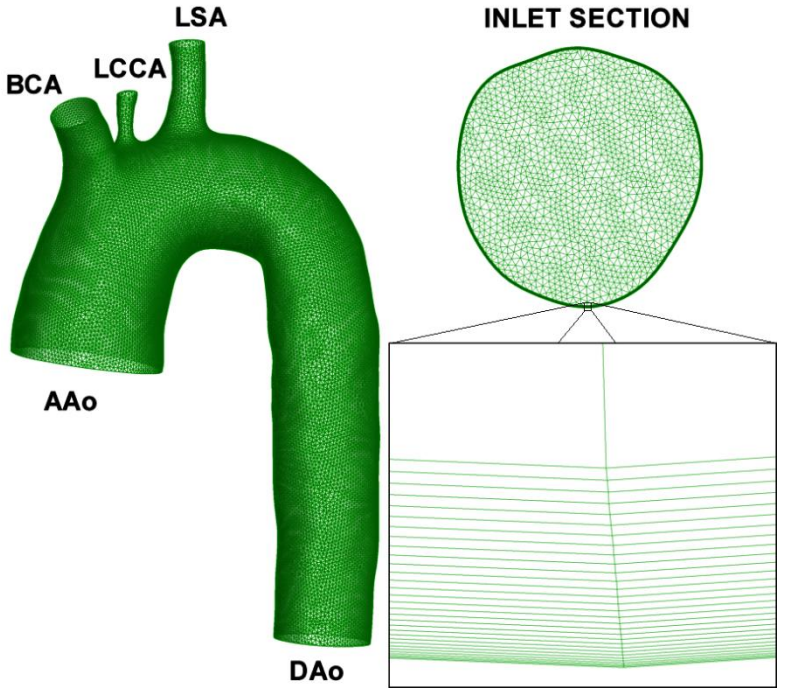

Figure 2.3 Resulting volume mesh of the investigating image-based computational model of a human thoracic aorta. Left panel shows mesh element size and density on the model wall; right panel display (top) the distribution of mesh cells on the inlet surface of the model (AAo) and (bottom) the near-wall refinement of the mesh with 30 prismatic cells layers.

Since the study is focused on the investigation of LDL transport and its transfer to the luminal surface, higher cell density was generated near the wall, defining 30 layers with prismatic elements (Figure 2.3). The highly accurate discretization of the boundary layer allows a better evaluation

of near-wall velocity gradients, ensuring a more accurate estimation of LDL transfer to the aortic wall and its correlation with WSS distributions. Mesh quality is a crucial factor, especially in modeling mass transport. For this reason, particular attention was put in this study in properly building up the mesh, in particular in properly setting the boundary layer. The quality of the mesh can be appreciated in Figure 2.3.

The grid was built up as in previous studies (Li et al., 2017), where the proper grid size at the inner wall surface is defined to appropriately model mass transfer to the wall, based on the Peclet number (Pe). The average Peclet number, used to indicate the relative proportion of convection to diffusion, is the product of the average Reynolds number (Re) and Schmidt number (Sc), as described by equation (2.1).

$$\mathrm{Pe} = \mathrm{Re} \cdot \mathrm{Sc} = \frac{D_h U}{\upsilon} \frac{\upsilon}{D_{LDL}} = \frac{D_h U}{D_{LDL}} \qquad (2.1)$$

where D_h and U are the hydraulic diameter (as measured from the reconstructed geometry) and the mean velocity value at the aortic inflow section averaged along the cardiac cycle, respectively. In this study, average Reynolds number was calculated to be approximately 1180, and D_{LDL}, the diffusivity

of LDL in flowing blood, was set to a constant value of $5.983 \cdot 10^{-12}$ $m^2 s^{-1}$ (Wada and Karino, 2002). The resulting average Peclet number was approximately $6.5 \cdot 10^8$. The design of the near-wall computational grid was driven by theory, applying an approach proposed by Tada in 2010. In detail, to properly model the advection *vs.* diffusion dominance in LDL transport phenomenon in aorta (with an average Pe = $6.5 \cdot 10^8$) a very refined near-wall computational grid is necessary, with a grid size dimension Δr_{max} close to the luminal surface defined as (Tada, 2010):

$$\Delta r_{max} = \frac{\delta_C}{3} = \frac{\delta}{3 \cdot \sqrt[3]{Sc}} = \frac{2.28 \cdot \sqrt{2\upsilon/\omega}}{3 \cdot \sqrt[3]{Sc}} \qquad (2.2)$$

$$Sc = \frac{\mu}{\rho \cdot D_{LDL}} = \frac{\upsilon}{D_{LDL}} \qquad (2.3)$$

where δ_C is the LDL boundary layer thickness, δ is the boundary layer thickness of the pulsatile flow, ω is the pulsation of the cardiac cycle, Sc is the Schmidt number, ρ is the density of blood, and μ and υ are the dynamic and kinematic viscosity, respectively. Based on equation (2.2), the largest near-wall grid side needed to appropriately describe the phenomenon under study is $92.7 \cdot 10^{-7}$ m. To be

conservative, here we set a near-wall grid size dimension equal to $3.4 \cdot 10^{-7}$ m. The adopted wall grid size dimension is about 27 times smaller than the largest near-wall grid side needed to appropriately describe the LDL transfer to wall. This choice has been conservatively valued to assure that the simulated data of LDL blood-to-wall transfer are not affected by the quality of the mesh grid.

In order to testify that the level of model discretization does not affect simulation results, the LDL concentration profile across the diameter of a defined cross section along the descending aorta was investigated. The aim of this analysis was to evaluate if mesh quality, with its change in cells density near the model wall, may produce discontinuity in the obtained solution for LDL transport in the bulk flow and its transfer to the luminal surface.

Low-density lipoproteins concentration values with respect to the defined DAo cross-section diameter, resulting from a steady-state performed simulation, are depicted in figure 2.4. LDL concentration values (C) have been normalized with respect to the physiological LDL concentration in whole blood (Yang and Vafai, 2006), equal to $2.86 \cdot 10^{-9}$ mol m^{-3} (C_0). The figure shows that no appreciable discontinuities affect the LDL concentration

profile: in the bulk flow region LDL concentration values are equal or very close to the mean physiological molecules concentration in blood; LDL concentration rises with continuity near to the vessel wall region displaying a relevant uptake of LDL, equal to the 7-8% with respect to C_0.

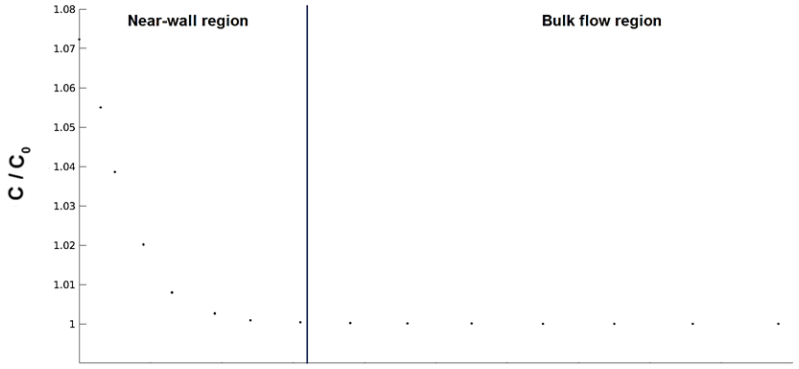

Figure 2.4 Resulting LDL normalized concentration profile with respect to a DAo cross-section diameter. Near-wall and Bulk flow regions are distinguished.

2.2 Numerical Approach

Transport of LDL in the streaming blood was modelled by coupling the governing (Navier-Stokes) equation of fluid

motion with the advection-diffusion equation under unsteady flow conditions.

2.2.1 Simulation assumptions

Blood was treated as a homogeneous, isotropic, incompressible, Newtonian viscous fluid with specific mass ρ equal to 1060 kg m^{-3} and dynamic viscosity μ set to a constant value of 3.5 cP (0.0035 Pa s).

Assuming that each component of the stress tensor $\bar{\bar{\boldsymbol{\tau}}}$ is a linear isotropic function of velocity gradient ($\boldsymbol{\nabla u}$) components, the following relation is valid for an incompressible fluid:

$$\bar{\bar{\boldsymbol{\tau}}} = 2\mu \boldsymbol{D}(\boldsymbol{u}) \qquad (2.4)$$

where ***D(u)*** is the rate of deformation tensor. Since the shear rate $\dot{\boldsymbol{\gamma}}$, which is also the gradient of the velocity vector, is related to the second invariant of $\boldsymbol{D}$, equation (2.4) explains that for a Newtonian fluid (1) the relation between shear stress and shear rate is linear and (2) the shear stress is directly proportional to the shear rate through the definition of a constant which is the dynamic viscosity of the fluid, as shown by equation (2.5).

$$\bar{\bar{\tau}} = \mu\dot{\gamma} \qquad (2.5)$$

Considering blood as a Newtonian fluid, with both constant density and dynamic viscosity, even if not reflecting the reality, could represent an acceptable and helpful assumption in specific analysing vascular domains. In detail, the assumption of Newtonian rheological behaviour of blood has to be verified considering both size and shear rate values characterizing the investigating domain. Modeling blood as a Newtonian fluid, in general, carries to negligible solution errors in vascular domain with larger diameters and exposed to higher shear rates. In fact, in small diameter blood vessels (less than 0.3 mm of cross section diameter), the characteristic dimension of blood cells, in particular red blood cells, becomes comparable with the diameter of the vessel itself: in this case, blood cells play an important role in determining the rheological behaviour of blood. Blood viscosity decreasing as the vessel diameter reduction (*plasma skimming*) is describes as Fåhræus–Lindqvist effect.

Moreover in vessels with low shear rates (less than 100 s^{-1}) the dynamic viscosity becomes a function of other parameters, such as velocity gradients, because red blood cells tend to aggregate forming bigger structures called *rouleaux*; since

these stacks of erythrocytes offer a greater resistance to blood flow, the viscosity increases with lower shear rates and the Newtonian fluid hypothesis falls.

The human thoracic aorta is the biggest vessel in circulatory system and exposed to high range of shear rate values over the cardiac cycle, so that, in the investigating vascular district, modeling blood even if representing a limitation, as a Newtonian fluid has been considered acceptable (as in previous studies, i.e. Gallo et al. 2012; Liu et al., 2011) .

Blood flow was considered to be laminar; no any strategy was applied to model turbulence, neglecting its effect on LDL transport and wall transfer. Generally different flow regimes can be characterized using the dimensionless quantity known as Reynolds number, which for flow in a pipe is defined as:

$$\mathrm{Re} = \frac{\rho U D}{\mu} \tag{2.6}$$

where D is the diameter of the AAo section of the investigating vascular domain. The physical meaning of Reynolds number is the relative importance of inertial and viscous forces for given flow conditions. Re can be interpreted as the ratio between the contribution of inertial

forces (ρUD) and the contribution of viscous forces (μ). Laminar flow occurs at low Reynolds numbers (usually Re < 2000) where the viscous forces predominate over the inertial ones.

From PC-MRI acquisitions, it was observed that the hemodynamics of the aorta under investigation is characterized by a mean Reynolds number equal to about 1180 at the inlet section of the ascending aorta. Re reaches values higher than 2000 in the systolic phase of cardiac cycle only, near the systolic peak of flowrate waveform (Figure 2.6). Resulting peak Reynolds number is equal to about 5000. Hence, flow in the aorta can destabilize during the deceleration phase of late systole, but even in this case there is a too short time period for the flow to become fully turbulent, so Reynolds numbers may reach the values of a few thousands thus falling in the range of transitional flow. Full scale turbulence may occur in some pathological states, such as vessel narrowing due to atherosclerosis, and defective heart valves.

Arterial wall was assumed to be rigid with no-slip condition at the wall. Straight flow extensions were added to the outlet sections of the model, in order to ensure a fully

developed flow and to minimize the effect of outlet boundary conditions on the solution (Gallo et al., 2012).

2.2.2 Fluid dynamic problem formulation

Governing equations of fluid motion are the Navier-Stokes momentum equation and the continuity equation. A discretized version of these equation has been solved through the investigating aortic domain by adopting a finite volume method.

More in detail, the investigating fluid domain Ω is represented by the lumen of the thoracic aorta, while the vessel walls, together with the inlet and outlet sections obtained by ideally cutting the vessel, form the boundaries of the domain, here indicated with Γ^{w}, Γ^{in} and Γ^{out}, respectively (Figure 2.5).

The governing equations expressed in differential form are:

$$\begin{cases} \dfrac{\partial(\rho \boldsymbol{u})}{\partial t} + \nabla \cdot \rho \boldsymbol{u}\boldsymbol{u} + \nabla p = \nabla \bar{\bar{\boldsymbol{\tau}}} + \rho \boldsymbol{f_v} & (2.7) \\ \dfrac{\partial \rho}{\partial t} + \nabla \cdot (\rho \boldsymbol{u}) = 0 & (2.8) \end{cases}$$

where $\boldsymbol{u}$ and p represent, respectively, the fluid velocity vector and the pressure, ρ is the blood density, $\rho \boldsymbol{f_v}$ represents the volume forces.

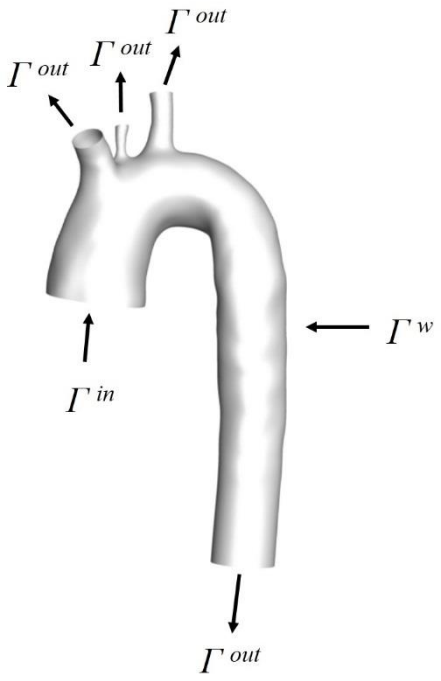

Figure 2.5 Image-based model of the aorta showing the boundaries (Γ^{w}, Γ^{in} and Γ^{out}) of the domain Ω.

Equation (2.7) is called the Navier-Stokes momentum equation and is derived from the momentum conservation equation extended to unsteady-state systems:

$$\begin{pmatrix} rate\ of \\ momentum\ accumulation \\ in\ the\ contol\ volume\ CV \end{pmatrix} =$$

$$\begin{pmatrix} rate\ of \\ momentum \\ entering\ CV \end{pmatrix} - \begin{pmatrix} rate\ of \\ momentum \\ leaving\ CV \end{pmatrix} + \begin{pmatrix} sum\ of\ forces \\ acting\ on \\ the\ system \end{pmatrix}$$

The left side of equation (2.7) describes the acceleration, while the right side of the equation is a summation of body forces, i.e. gravity, and divergence of deviatory stress.

Equation (2.8) represents the most general form of the mass continuity equation, which simply states that the rate of mass accumulation in a control volume (*CV*) is exactly the summation of the mass entering rate and the rate of mass leaving the *CV*:

$$\begin{pmatrix} rate\ of \\ mass\ accumulation \\ in\ the\ contol\ volume\ CV \end{pmatrix} = \begin{pmatrix} rate\ of \\ mass \\ entering\ CV \end{pmatrix} - \begin{pmatrix} rate\ of \\ mass \\ leaving\ CV \end{pmatrix}$$

Assuming a Newtonian behavior for blood the above equations ((2.7) and (2.8)) are altered; in particular, fluid

density and dynamic viscosity are assumed to be constant, so that the term $\nabla\bar{\bar{\tau}}$ becomes equal to $\mu\nabla^2\boldsymbol{u}$.

Resulting governing equations of fluid motion are then simplified as follows:

$$\begin{cases} \rho\left[\dfrac{\partial \boldsymbol{u}}{\partial t} + \boldsymbol{u}(\nabla\cdot\boldsymbol{u})\right] = -\nabla p + \mu\nabla^2\boldsymbol{u} + \rho\boldsymbol{g} & (2.9) \\ \nabla\cdot\boldsymbol{u} = 0 & (2.10) \end{cases}$$

where the term representing the volume forces is consider to consist of the gravity force only.

The result is a set of coupled, non-linear, partial differential equations where the unknown variables are the blood velocity vector $\boldsymbol{u}$ and the pressure p; these equations are defined in a computational domain representing a specific location in the space, through which the fluid flows as time passes (Eulerian approach).

2.2.3 LDL transport problem formulation

LDL was assumed to be present in dissolved form in blood and it was modelled as a passive non-reacting scalar, transported in the streaming blood according to the advection-diffusion equation:

$$\frac{\partial \mathrm{C}}{\partial \mathrm{t}} + \boldsymbol{u} \cdot \nabla \mathrm{C} - D_{LDL} \nabla^2 \mathrm{C} = 0 \qquad (2.11)$$

where C is the LDL blood concentration, $\boldsymbol{u}$ is the velocity vector obtained from the flow the solution of Navier-Stokes equations. More in detail, $\frac{\partial C}{\partial t}$ is the non-stationary or transient term, describing the time-dependent behavior of advective-diffusive system; $\boldsymbol{u} \cdot \nabla C$ is the advective/convective term and describes the change in LDL concentration at a given location because of the flow; $-D_{LDL} \nabla^2 C$ term represents the diffusive term, it describes the transport of LDL particles in flowing blood due to diffusion and it is proportional to the Laplacian (or second derivative) of concentration C.

Technically, solving mass transport equation in CFD code Fuent requires the definition of a *User-Defined Scalar* (*uds*), a scalar representing the LDL concentration in the entire fluid domain (C in equation (2.11)). The *uds* transport equation was then customized by setting the parameter D_{LDL}, which represents the *uds* diffusivity in blood, to $6.3 \cdot 10^{-9}$ kg m^{-1} s^{-1}.

2.2.4 Conditions at boundaries

To solve coupled fluid dynamic and mass transport equations an appropriate set of boundary conditions on the investigating vascular domain has to be prescribed (Figure 2.1). The border of the analyzing model ($\partial\Omega$) consists of six different surfaces, as shown by figure 2.5: Γ^{w} corresponds to the physical border represented by the arterial wall, while the inlet and outlets of the model are fictitious surfaces arbitrarily chosen by clipping the geometric model perpendicularly to the vessel centerlines, thus separating the vessel from the rest of the circulatory system. In particular, Γ^{in} represents the inlet or inflow boundary, i.e. the section closest to the heart along the main direction of blood flow; the outlets or outflow boundaries of the model are generally denoted with Γ^{out}, and were obtained again by clipping the four different outlets, i.e. the brachiocephalic artery (Γ^{BCA}), the left common carotid artery (Γ^{LCCA}), the left subclavian artery (Γ^{LSA}) and the descending aorta (Γ^{DAo}), perpendicularly to every vessel centerline.

The following two sections will discuss about the BCs imposed in order to close the problem and solve the equations of fluid motion and mass transport.

2.2.4.1 Boundary conditions for fluid dynamics

The arterial wall was assumed to be rigid with no-slip condition (null fluid velocity) at the wall.

Flow rate waveform were measured at all the vessels in the investigating domain. The time-dependent trend of blood flow rates measured along the cardiac cycle is reported in figure 2.6. In detail, the time axes is normalized with respect to the subject-specific cardiac period T equal to 1.111 s, corresponding to a cardiac rate of 54 bpm. The flow was determined in PC-MRI slices perpendicular to the centerline of both the aorta and the supra-aortic vessels. The centerline was identified as the line connecting the centers of the luminal contours, obtained from the axial slices of the magnitude image. Then, at a plane perpendicular to the vessel centerline, velocities were extracted from the phase images and integrated to obtain the flow rate waveforms.

While flow rate profiles at the inlet section of the aortic model (AAo) and at the outlet section along the descending aorta (DAo) where directly defined starting from PC-MRI measured data, flow rate waveforms at each supra-aortic branch was computed by difference between flow rate measured at two different sections of the aortic arch placed immediately upstream and immediately downstream with

respect to the branching, as in previous studies (i.e., Gallo et al., 2012). This strategy ensures the instantaneous mass conservation constraint at the acquisition instants.

Two different BC strategies were applied at the inlet section of the AAo. The first strategy consists in the application of the measured PC-MRI 3D velocity profiles at the AAo inlet section. Phase-contrast flow maps were used to obtain pixel-based time-varying velocities and to generate Dirichlet inflow BCs, applied in terms of 3D velocity profiles (BC_{3D}) at the ascending aorta (AAo) inlet section (as detailed in Morbiducci et al., 2013). In detail, at the AAo inlet section the measured three components of the velocity vector were extracted from the phase images. As a result, every voxel of the inlet section was equipped with a velocity vector whose direction and magnitude was determined from the PC-MRI data. The inflow condition was generated by imposing at the inlet of the ascending aorta PC-MRI measured 3D velocity profiles at each instant of cardiac cycle. The velocity profiles extracted along the cardiac cycle was prescribed as inlet BC in the computational model by applying a surface-fitting algorithm of the measured data (Leuprecht et al., 2003). Explanatory examples of the PC-MRI-derived axial velocity component, applied as inflow BCs, averaged along systole, diastole and

along the whole cardiac are provided by figure 2.6 (bottom panel).

The second strategy is a widely applied approach and consists in the application of the measured flow rate waveform (obtained by integration of the PC-MRI velocities at the AAo inlet section) in terms of idealized flat velocity profiles (BC_F), an assumption dictated by the lack of knowledge on the real profile associated to the measured flow rate. In detail, the inflow conditions were generated by dividing the measured data of inlet flow rate by the inlet section of the ascending aorta, for each instant of the cardiac cycle.

In this study the investigation, regarding inflow BC effect on results, was limited to the flat velocity profile, as idealized inlet BC at the ascending aorta, not considering the impact of using the parabolic profile, the fully developed profile or the Womersley analytical solution as Dirichlet boundary condition at the inflow section. The reason for this choice is in the fact that: (1) a flat or fully developed profile is still the most widely adopted assumption in aorta (Wen et al., 2010; Liu et al., 2009, 2011; Gallo et al., 2012; Brown et al., 2012); (2) previous findings suggest to use plug flow (Reymond et al., 2009; Marzo et al., 2009), when an idealized flow must be

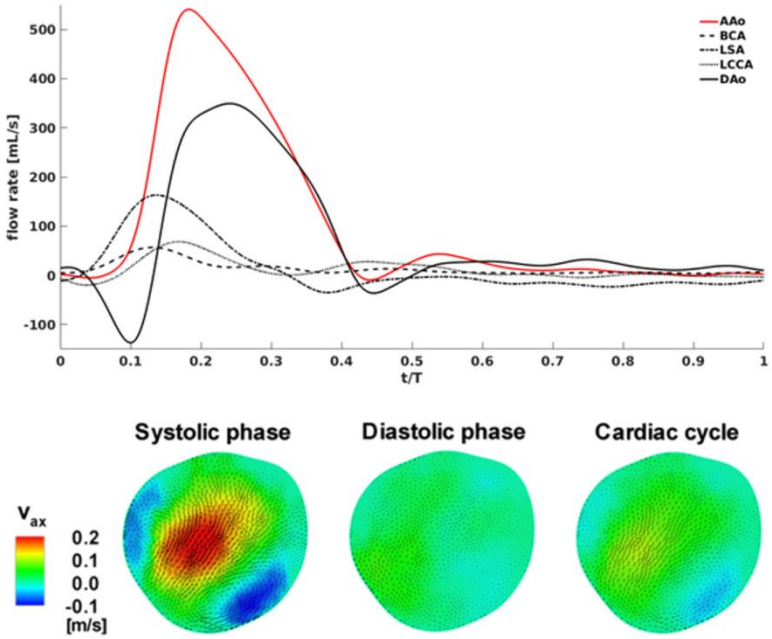

Figure 2.6 Explanatory examples of contours of the PC-MRI-derived axial velocity component, applied as inflow BCs, averaged along systole, diastole and along the whole cardiac cycle (maps also show the structure of secondary flows in terms of in-plane velocity vectors, arrows not scaled). Flow rate waveforms at outflow and inflow boundaries are also presented. AAo-ascending aorta; Dao-descending aorta; BCA-brachiocephalic artery; LCCA-left common carotid artery; LSA-left subclavian artery.

prescribed as inflow boundary condition; (3) it has been demonstrated that, in aorta, the simulated hemodynamics obtained prescribing a fully developed velocity profile as

inflow boundary condition does not satisfactorily agrees with the one obtained prescribing 3D PC-MRI measured velocity profiles (Morbiducci et al., 2013).

Using parabolic velocity profiles (which is the law of fluid motion proposed by the Hagen-Poiseuille theory) as inflow boundary condition is widely considered an unacceptable idealization in the ascending aorta (due to the flow regimes and geometry) and it has been never applied to image-based computational models of the aortic hemodynamics.

As regards the outlet sections of the model, PC-MRI measured flow rates (Figure 2.6) were prescribed as outflow BCs. In detail, fixed flow rate ratio distributions at the DAo, BCA, LCCA and LSA outlet sections were derived from measured flow rate waveforms by imposing the flow rate at each outlet to a constant fraction of the inlet flow rate waveform: this fixed fraction corresponds to the ratio between the time-averaged flow rate measured at that outlet and the time-averaged flow rate measured at the inlet section (Gallo et al. 2012). The constant outflow ratios used as BCs for this study are presented in Table 2.1.

Table 2.1: Flow rate ratios applied as outflow boundary conditions.

OUTFLOW RATE RATIOS	
BCA	13%
LCCA	10%
LSA	13%
DAo	64%

2.2.4.2 Boundary conditions for mass transport

To solve equation (2.11), a uniform LDL concentration profile C_0 equal to $2.86 \cdot 10^{-9}$ mol/m^3, corresponding to the physiological LDL concentration in whole blood (Yang and Vafai, 2006), was prescribed at the AAo inflow section. At each outlet segment of the aorta, the gradient of LDL concentration along the vessel was set to zero. At each outflow sections of the fluid domain, the gradient of LDL concentration along the vessel was set to zero. In detail, a homogeneous Neumann condition, i.e. a zero

flux condition for LDL ($\frac{\partial C}{\partial n}$=0, where n is the normal to the outflow section) is "a reasonable approximation, especially for the high Peclet number flows characterizing arterial mass transport in arteries. Such boundary condition is known to be relatively ''benign'' and do not contaminate the solution field inside the computational domain" (Ethier, 2002).

To model the LDL blood-to-wall transfer the following equation was imposed at the luminal surface:

$$C_W V_W - D_{LDL} \left.\frac{\partial C}{\partial n}\right|_W = K_W C_W \qquad (2.12)$$

where C_W is the LDL concentration at the vessel wall, i.e., at the endothelial surface; V_W the water filtration velocity at the wall, i.e., the transmural component of the fluid velocity at the wall (set equal to $4 \cdot 10^{-8}$ m/s); $\partial C/\partial n$ is the concentration gradient normal to the wall (with n indicating the direction normal to the luminal surface); and K_W is the overall mass transfer coefficient of LDL at the vessel wall ($K_W=2 \cdot 10^{-10}$ m s^{-1} (Wada and Karino, 2002)).

Equation (2.12) is "a mass balance at the wall-blood interface, and it states that the amount of LDL infiltrating into the vessel wall is the difference between the amount carried to the vessel wall by filtration flow and the amount that diffuses

back to the mainstream" (Deng et al., 1995). In detail, equation (2.12) specifies a solute flux entering the wall in terms of a blood-side solute concentration at the wall and an endothelial permeability function. In this study, the second term of equation (2.12), representing the net flux of LDL into the arterial wall, was assumed to be negligible, a widely accepted first-order approximation (Deng et al., 1995; Li et al., 2017; Liu et al., 2009).

This assumption is based on previous numerical and experimental observations (Deng et al., 1995), and on reported values for K_W (Wada and Karino, 2002; Bratzler et al., 1977; Truskey et al., 1992), which are two order of magnitude lower than V_W ($V_W=4\cdot10^{-8}$ m s^{-1} vs. $K_W=2\cdot10^{-10}$ m s^{-1}). As a consequence, in equation (2.12) it will result to be: $\frac{K_W C_W}{C_W V_W} \sim 10^{-2}$. Being the term at second member in equation (2.12) two order of magnitude lower than the LDL filtration term, the assumption done can be considered acceptable.

2.2.5 LDL initial conditions

Coupled with the two applied strategies of inflow BCs, four different initial distributions of LDL were imposed for the unsteady-state simulations (Figure 2.1). More in detail, two first strategies consisted in the imposition as initial LDL

distributions in the whole domain the one resulting from steady-state simulations where the averaged measured flow rate at the AAo section was applied in terms of averaged measured 3D velocity profile (IC_{3D}), or flat velocity profile (IC_F). Two other strategies consisted in the initialization of the LDL concentration to a uniform and constant value $C=C_0$ (IC_U) or $C=0$ (IC_N) in the whole domain. Figure 2.7 displays the four imposed strategies of ICs, highlighting differences in LDL wall distribution among the four cases.

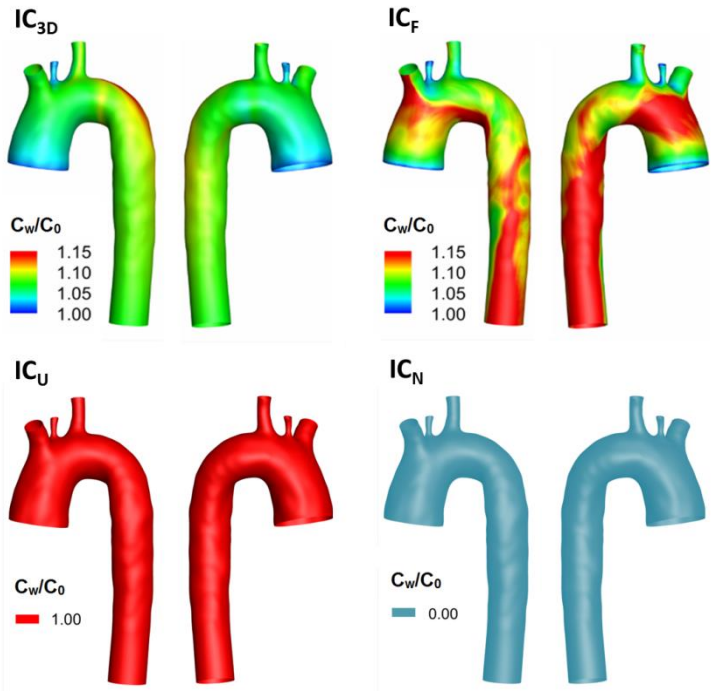

Figure 2.7 Four imposed LDL initial distribution in the whole investigating domain.

2.2.6 Technical computational settings

Summarizing two steady-state simulations were performed to define a subset of LDL concentration initial conditions, and eight unsteady-state simulations were conducted in order to investigate the impact of each imposed initial and boundary condition on transport and wall transfer of LDL in the investigating domain (Table 2.2).

Table 2.2: Summary of the eight unsteady-state simulated cases, characterized by the prescription of different initial condition strategies for LDL profile at the aortic wall.

	BOUNDARY CONDITION	
INITIAL CONDITION	**BC_{3D}**	**BC_F**
IC_{3D}	BC_{3D}-IC_{3D}	BC_F-IC_{3D}
IC_F	BC_{3D}-IC_F	BC_F-IC_F
IC_U	BC_{3D}-IC_U	BC_F-IC_U
IC_N	BC_{3D}-IC_N	BC_F-IC_N

All the possible combinations of BC-IC were investigated in order to obtain a complete analysis of the investigating

effect of boundary and initial conditions on LDL transport and wall transfer in personalized model of human aorta. Moreover, the choice to simulate also heterogeneous couples (i.e. BC_{3D}-IC_F and BC_F-IC_{3D}) could result helpful in reducing computational cost or overcoming problems related to measured clinical data unavailability.

Second order accuracy was prescribed to solve both the momentum equation and pressure. The discretisation scheme applied to the solution of the advection-diffusion equation was the second order upwind scheme, as suggested elsewhere (Carroll et al., 2010). The second order upwind scheme was chosen, in order to achieve higher-order accuracy at cell faces by computing quantities using a multidimensional linear reconstruction approach; in addition to that, the Green-Gauss Cell Based option was used as method for gradient computing.

The pressure-velocity coupling method SIMPLE was used for all the simulations. Under-relaxation factors have been set up to control the update of computed variables at each iteration, thus improving the stability of the solution. In detail, under-relaxation factors equal to 0.3 and 0.7 were chosen respectively for pressure and momentum, while for

density, body forces and *uds* the under-relaxation factors were set to 1.

The backward Euler implicit scheme was adopted for time integration, with a fixed 1 ms time increment. The measured cardiac rate of 54 bpm was simulated. Convergence was achieved when the maximum mass, momentum and species residuals fell below 10^{-4},10^{-4} and 10^{-9}, respectively.

Simulations were run for a sufficient number of cycles to damp initial transients (20 cycles on average). More in detail, The independence of each simulation from the prescribed initial LDL concentration was achieved as follows: a number of cardiac cycles *N* was simulated until the maximum local percentage difference in LDL concentration between cycle *i* and cycle *i+1* (*i*=1,….*N*-1) was lower than 1%.

2.2.7 WSS-based descriptors and co-localization

Near-wall hemodynamics was evaluated in terms of "established" WSS-based descriptors. In detail, the distributions at the luminal surface of the vessel of three of the most widely used WSS-based descriptors, i.e. the Time-Averaged Wall Shear Stress magnitude (TAWSS), Oscillatory Shear Index (OSI) (Ku et al., 1985), and Relative Residence Time (RRT) (Himburg et al., 2004) were computed as:

$$\mathrm{TAWSS} = \frac{1}{T}\int_0^T |\mathbf{WSS}| \cdot dt \tag{2.13}$$

$$\mathrm{OSI} = 0.5\left[1 - \left(\frac{\left|\int_0^T \mathbf{WSS} \cdot dt\right|}{\int_0^T |\mathbf{WSS}| \cdot dt}\right)\right] \tag{2.14}$$

$$\mathrm{RRT} = \frac{1}{\mathrm{TAWSS} \cdot (1 - 2 \cdot \mathrm{OSI})} = \frac{1}{\frac{1}{T}\left|\int_0^T \mathbf{WSS} \cdot dt\right|} \tag{2.15}$$

where *T* is the overall cardiac cycle and **WSS** is the wall shear stress vector.

TAWSS, OSI and RRT are widely accepted indicator of "disturbed" shear: low values of TAWSS are known to induce proatherogenic endothelial phenotype (Malek et al., 1999); high values of OSI identify regions at the vessel wall interested by a persistent deviation of the instantaneous WSS from the main flow direction, inducing perturbed endothelial alignment (He and Ku, 1996); RRT, a combination of TAWSS and OSI, is proportional to the residence time of blood particles near the wall. RRT is a robust single metric of low and oscillating shear.

Additionally, WSS multidirectionality was evaluated considering emerging descriptors of multidirectional shear. More in detail, three other WSS-based descriptors, counting

the multidirectionality of WSS vector over all the cardiac cycle, where computed: transverse WSS (transWSS), defined as the WSS component acting perpendicularly to the time-averaged WSS vector direction (Peiffer et al., 2013); the cycle-average values of the projections of WSS vector respectively along (1) the "axial direction" ($\mathbf{WSS}_{ax}$), identified as the direction of the tangent to the vessel centreline, and (2) the secondary direction ($\mathbf{WSS}_{sc}$), orthogonal to the axial direction and related to secondary flow (Morbiducci et al., 2015). transWSS, $\mathbf{WSS}_{ax}$ and $\mathbf{WSS}_{sc}$ distributions at the lumen surface were obtained as:

$$\text{transWSS} = \frac{1}{T}\int_0^T \left| \mathbf{WSS} \cdot \left(\mathbf{n} \times \frac{\int_0^T \mathbf{WSS} \cdot dt}{\left| \int_0^T \mathbf{WSS} \cdot dt \right|} \right) \right| \cdot dt \quad (2.16)$$

$$\mathbf{WSS}_{ax} = \frac{\mathbf{WSS} \cdot \mathbf{C}'}{|\mathbf{C}'|} \frac{\mathbf{C}'}{|\mathbf{C}'|} \quad (2.17)$$

$$\mathbf{WSS}_{sc} = \frac{\mathbf{WSS} \cdot \mathbf{S}}{|\mathbf{S}|} \frac{\mathbf{S}}{|\mathbf{S}|}; \quad \mathbf{S} = \frac{\mathbf{C}' \times \mathbf{R}}{|\mathbf{C}'||\mathbf{R}|} \quad (2.18)$$

where **WSS** is the WSS vector; **n** is the unit vector normal to the arterial surface; **C'** is the tangent vector to the centerline

C, **R** is the vector orthogonal to **C'** associating the generic point on the arterial wall to the centerline. A clarifying illustration of axial and secondary WSS is provided by figure 2.8.

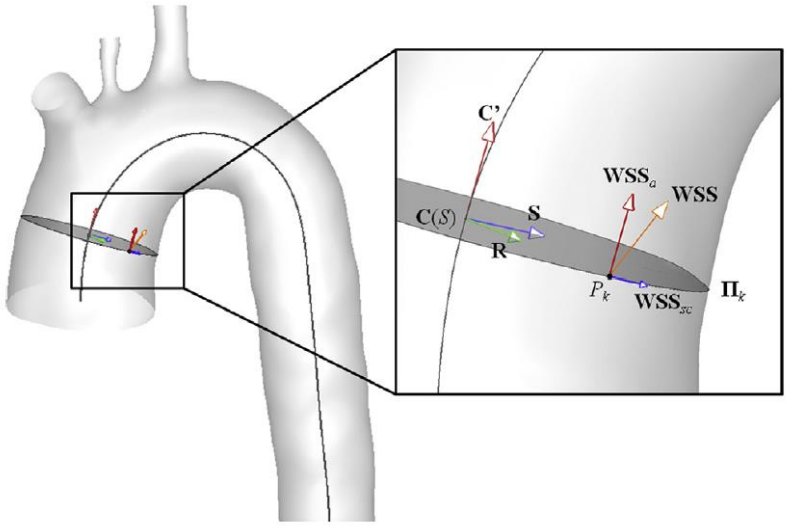

Figure 2.8 Projection of the local **WSS** vector at the generic point P_k at the vessel wall (1)along the axial direction, **WSS**$_{ax}$, and (2)the secondary direction, **WSS**$_{sc}$, related to secondary flow on plane Π_k (orthogonal to the centerline) point Pk belongs to (from Morbiducci et al., 2015).

To determine objective thresholds for 'disturbed' shear, the same scheme as proposed in 2008 by Lee et al., and as applied in several studies also by the research group to which

I belong in carotid bifurcations (Gallo et al., 2012; Gallo et al., 2016), and in aorta (Morbiducci et al., 2013; Morbiducci et al., 2015), was applied. Technically, data from all cases where BC_{3D} inflow condition were applied (assuming this one closer to the physiological condition), were pooled to identify the lower 20^{th} percentile value of TAWSS, and upper 20^{th} percentile values of OSI, RRT, and transWSS. Disturbed shear was quantified as the surface area (SA) exposed beyond (below for TAWSS) these percentile values. According to previous studies (Lee et al., 2008; Lee et al., 2009; Hoi et al., 2010; Zhang et al., 2010; Bijari et al., 2012), SAs exposed to disturbed flow are here referred as TAWSS20, OSI80, RRT80 and transWSS80.

As concerns $\mathbf{WSS}_{ax}$ and $\mathbf{WSS}_{sc}$, the SA with cycle-average $\mathbf{WSS}_{ax}$ magnitude aligned with (opposite to) the local tangent to the centerline of the vessel was denoted as WSS_{ax}^{+} (WSS_{ax}^{-}), and the SA with cycle-average $\mathbf{WSS}_{sc}$ magnitude left-handed (right-handed) direction over a vessel cross-section was denoted as WSS_{sc}^{lh} (WSS_{sc}^{rh}).

Finally, in order to evaluate the impact of the imposed BC-IC strategies, a co-localization analysis was conducted. In detail, the overlap of higher LDL polarization areas at the vessel wall with every identified SA of “disturbed” shear,

basing on WSS-based descriptors distribution, at the luminal surface was also performed (Gallo et al., 2016). To do this, an objective threshold for the normalized LDL concentration at the vessel wall (C_W/C_0) was determined by pooling data from the four simulated cases with imposed BC_{3D} (Table 2.2). Then the 80^{th} percentile value of C_W/C_0 at the luminal surface was identified and the surface area of the vessel wall exposed beyond this percentile value was denoted as LDL80. The co-occurrence was evaluated by quantifying the spatial overlap of defined SAs exposed to respective thresholds of disturbed shear and LDL80.

Chapter 3

Results

3.1 Computational cost

Computational cost needed to achieve the independence of the single simulated cardiac cycle from the imposed initial LDL concentration is reported in Table 3.1. The table lists the number of simulated cardiac cycles needed to achieve the simulation solution, independent from the prescribed initial condition.

It can be observed that the application of different BC-IC strategies carries to markedly different computational costs, ranging between 6 and 61 when, respectively, BC_{3D}-IC_{3D} and BC_F-IC_F strategies are applied as B-I conditions. Moreover, it

can be noticed that, in general, (1) inflow BC_{3D} ensures lower computational costs to reach independence from the IC (with the exception of IC_U) and (2) the application of IC_N as initial LDL concentration carries to the higher computational costs, independent of the inflow boundary condition (57 and 61 simulated cardiac cycles when, respectively, BC_{3D} and BC_F are applied as inflow BC).

Table 3.1: Number of cardiac cycles simulated to damp initial transient for each of the eight unsteady-state simulated cases

	BOUNDARY CONDITION	
INITIAL CONDITION	**BC_{3D}**	**BC_F**
IC_{3D}	6	18
IC_F	7	16
IC_U	10	10
IC_N	57	61

3.2 LDL wall distribution

Looking at the high computational costs related to the conducted unsteady-state simulations, in order to justify the choice of unsteady-state simulations instead of steady-state ones, percentage differences between obtained results, in terms of wall LDL normalized distribution, when the two different simulation strategies are applied, are displayed in figure 3.1. In detail, the figure shows the percentage differences between the obtained values of LDL normalized concentration at the luminal surface when BC_{3D}-IC_N is applied as BC-IC strategy and, respectively, steady-state and unsteady-state simulations are conducted. Computed percentage differences values (between the two different simulated cases) range between 95% and 100% over all the model surface, with the higher values on the posterior part of the aortic arch and along the posterior part of the DAo.

Figure 3.2 shows the obtained normalized cycle-averaged LDL concentration profiles at the luminal surface for the eight conducted simulations. It can be noticed that depending on the prescribed BC-IC strategy, a different LDL concentration profile at the vessel's wall results, both in terms of location (depending on the applied BC-IC strategy, different zones on the luminal surface are interested by a higher uptake of LDL)

and polarization value. In detail, concerning location along the vessel wall interested by higher concentration of LDL, depending on the applied BC-IC strategy different zones of the luminal surface are indicated as pro-atherogenic (characterized by a higher value of normalized LDL concentration).

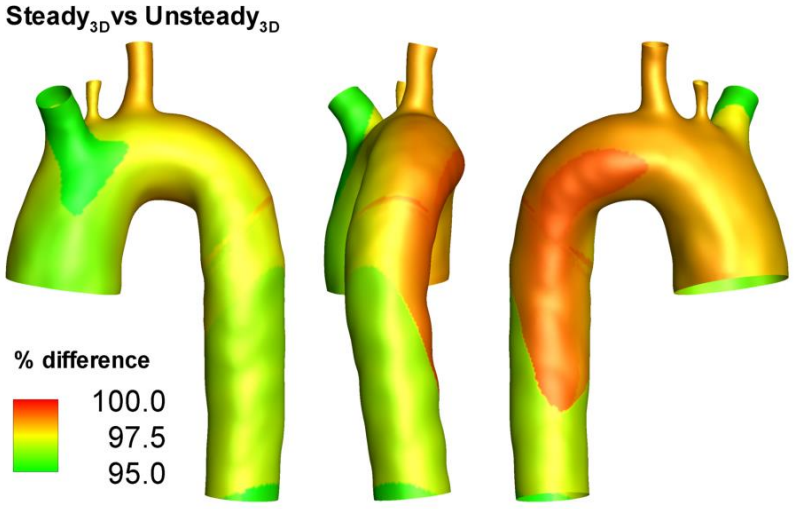

Figure 3.1 Percentage differences between normalized LDL distributions at the luminal surface obtained for steady vs. unsteady BC_{3D}-IC_N case simulations.

In particular, focalizing the attention on the independence of the applied boundary condition, the imposition of different initial conditions results in the individuation of different pro-

atherogenic locations: the extrados of the aortic arch and little regions along the outer part of the DAo when IC_{3D} is applied; the inner part of the BCA, the intrados of the aortic arch and relevant regions along the DAo when IC_F is prescribed; no well-defined pro-atherogenic locations when IC_U is applied; the inner part of the BCA, small regions in the intrados of the aortic arch and along the DAo when IC_N is applied (Figure 3.2).

Concerning the role played by the imposed boundary condition, figure 3.2 shows an extension of vessel's wall areas interested by LDL polarization for BC_F cases with respect to BC_{3D} ones. In detail, comparing obtained LDL distributions at the luminal surface of the model, regardless of the prescribed initial condition, the imposition of BC_F as inflow results (1) in wider pro-atherogenic aortic SAs with respect to the corresponding BC_{3D} case when IC_{3D}, IC_F and IC_N are applied as initial condition and (2) in a less evident increase of pro-atherogenic luminal SAs when IC_N is prescribed, which is focalized around the inlet surface of the model (AAo) and at the intrados of the aortic arch.

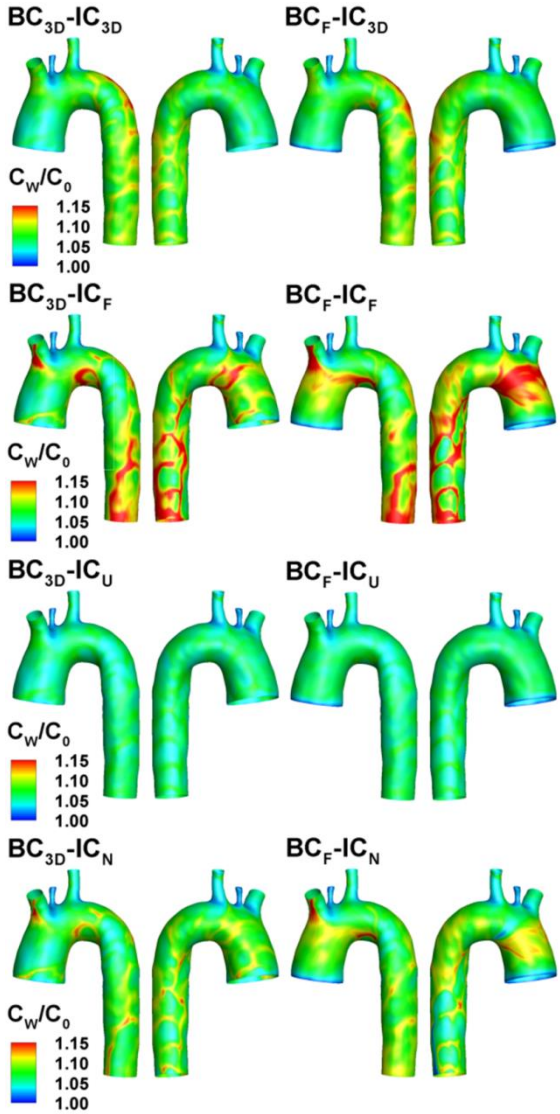

Figure 3.2 Impact of BC-IC strategies on LDL concentration polarization: normalized LDL concentration profiles at the aortic luminal surface (two different views).

As regards differences in resulting LDL polarization value, depending on the prescribed BC-IC strategy, figure 3.2 points out that, independently of the applied BC, (1) an uneven cycle-averaged LDL polarization at the luminal surface occurs when IC_{3D}, IC_F and IC_N strategies are prescribed, with local values up to the 15% higher than C_0, the mean LDL concentration in the blood, while (2) a relatively uniform LDL concentration, close to C_0, is obtained at the vessel wall considering IC_U.

A more quantitative evaluation of the overall effect of the imposed inflow BC strategy is given by figures 3.3 and 3.4. In particular, figure 3.3 highlights the impact of the imposed boundary condition in determining the normalized LDL concentration value at the vessel wall by showing the absolute value of percentage differences of the local LDL concentration values at the luminal surface calculated with respect to the inflow BC_{3D} cases, here considered the reference standard. Percentage values lower than 2% are not displayed. It can be noticed that, generally, the imposition of a BC_F as inflow leads to LDL polarization values at the wall mainly between 4% and 8% different with respect to the reference cases. Higher values of percentage differences are observed when IC_F and IC_N are prescribed as initial condition

for the LDL distribution in the model, and are mainly focalized in three areas of the model's wall: the ascending part, the intrados and the descending part of the aortic arch, all showing percentage difference peaks up to the 10%. Less relevant values of percentage differences (lower than 5%) are obtained for the other cases (IC_{3D} and IC_U) with only some focal peaks of 4.5% at the intrados of the vessel when IC_{3D} is applied (Figure 3.3).

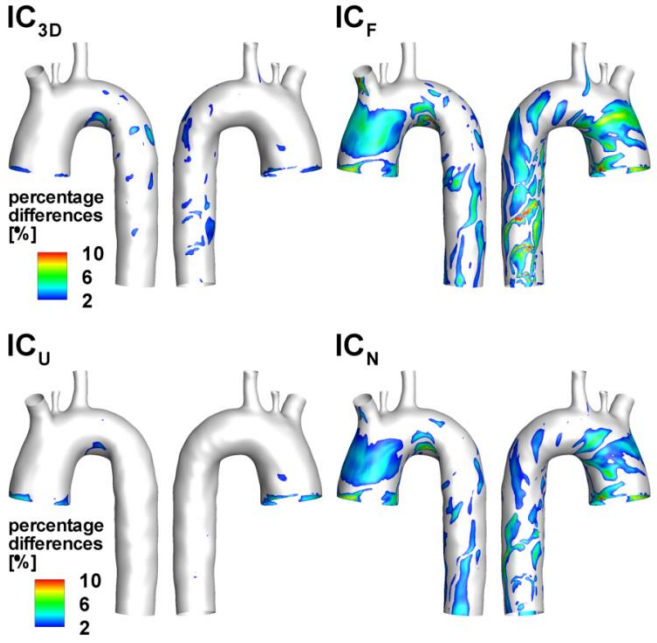

Figure 3.3 Impact of BC strategies on normalized LDL concentration at the vessel wall: percentage differences of normalized LDL distributions at the luminal surface for every investigated initial condition, calculated with respect to the inflow BC_{3D} cases (two different views).

Going deeper in the investigation of the impact of the imposed inflow BC strategy, figure 3.4 presents the probability density functions (PDFs) of the percentage differences, with their positive or negative sign, of the local LDL concentration values at the vessel's wall, for every IC.

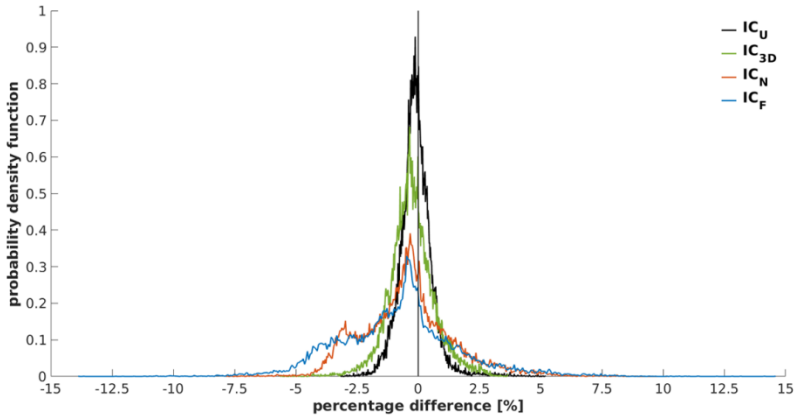

Figure 3.4 Probability density functions (PDFs) of the percentage differences of the local LDL polarization values at the vessel wall. For each investigated initial condition, percentage differences are calculated with respect to the inflow BC_{3D} case.

Table 3.2 reports the reference values describing the PDFs displayed in figure 3.4. In detail, skewness, mean and median values, computed for each IC, are listed. Moreover, the probabilities that the percentage difference distribution

assumes a negative or a positive value are reported and respectively indicated with $P^{[-,0\%]}$ and $P^{[0\%,+]}$.

All the PDFs exhibit an asymmetric unimodal trend. All the distributions are characterized by positive values of skewness (Table 3.2) with their right tails longer than the left ones and with their mass concentrated on the left (the negative part) of the figure 3.4. Moreover, all the PDFs are characterized by negative mean and median values (Table 3.2).

Table 3.2: Statistical parameters of PDF

INITIAL CONDITION	**skewness**	**mean**	**median**	$\mathbf{P^{[-,0\%]}}$	$\mathbf{P^{[0\%,+]}}$
$\mathbf{IC_{3D}}$	0.05	- 0.26	- 0.29	65 %	35 %
$\mathbf{IC_{F}}$	0.29	- 0.81	- 0.69	68 %	32 %
$\mathbf{IC_{U}}$	1.01	- 0.09	- 0.12	60 %	40 %
$\mathbf{IC_{N}}$	0.50	- 0.46	- 0.46	65 %	35 %

The previous observations indicate that the imposition of a BC_F as inflow, rather than the more realistic BC_{3D}, carries to a larger LDL uptake over the luminal surface (Figure 3.4). More in detail, looking at the probability values $P^{[-,0\%]}$ and $P^{[0\%,+]}$ (Table 3.2), it can be noticed that the amount of the vessel's wall interested by a greater LDL transfer when BC_F is applied as inflow, with respect to the BC_{3D} case, is bigger that the 60%, independently of the imposed initial condition. Moreover, investigating the impact of the prescribed IC, the largest value of luminal surface interested by a higher amount of LDL uptake, when BC_F is prescribed as inflow, is obtained for IC_F case and is equal to 68%.

PDFs in figure 3.4 also show that percentage differences are mainly distributed in the range ±3% for IC_U and IC_{3D} cases and in the range ±6% for IC_N and IC_F cases, as expected from figures 3.2 and 3.3. In detail, the percentage area under the PDF between -3% and +3% is equal to 99.5% for the IC_U case and 99.2% for the IC_{3D} case, highlighting that the role played by the prescribed BC strategy is less relevant in these two cases and only related with some focal peak values of percentage differences up to 5% (as shown in both figures 3.3 and 3.4). More significant is the investigation of the impact of the imposed BC strategy when IC_N and IC_F are prescribed as

initial conditions. In these cases, computed percentage differences values are higher (than the previous cases): it has to be selected the range ±6% to obtain values of percentage area under the PDF equal to 99.4% and 97.4% for IC_N and IC_F case, respectively. Moreover, it can be observed focal values of percentage differences up to 14.5% for the IC_F case (Figure 3.4).

Figure 3.5 shows the obtained percentage values of LDL80 aortic surface area for all the eight simulated cases.

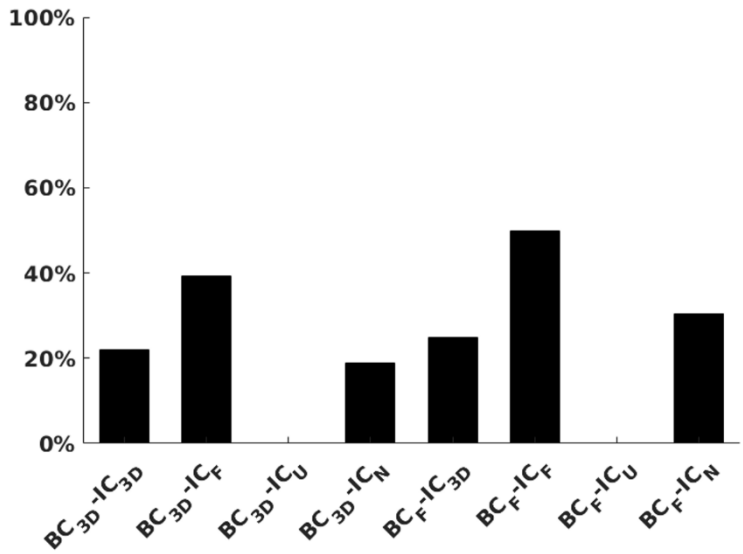

Figure 3.5 Quantitative analysis of the impact of BC-IC strategies on LDL concentration polarization: percentage of LDL80 aortic surface area.

It can be noticed that obtained LDL80 aortic SA is equal to zero when a uniform LDL distribution (equal to C_0) is prescribed as IC, independently of the inflow boundary condition.

The largest relative LDL80 aortic SA is produced by the imposition of IC_F as initial condition, independently of the inflow BC. More in detail, for cases in which BC_{3D} is prescribed as inflow BC, the imposition of IC_F produces a percentage value of LDL80 aortic surface area equal to 39.2%; for cases in which BC_F is prescribed as inflow BC, the imposition of IC_F produces a percentage value of LDL80 aortic surface area equal to 50.0% (Figure 3.5). Neglecting IC_U cases, the lowest values of LDL80 aortic SA are produced (1) by the prescription of IC_N as initial condition, when BC_{3D} is applied as inflow boundary condition, and (2) by the imposition of IC_{3D} as initial condition, when BC_F is applied as inflow boundary condition. In detail, obtained percentage values of LDL80 aortic surface area are equal to 18.9% and 30.5% for BC_{3D}-IC_N and BC_F-IC_{3D} cases, respectively (Figure 3.5).

Moreover, looking at figure 3.5 it can be noticed that, in general, comparing obtained results for cases with the same

prescribed initial condition, the imposition of BC_{3D} as inflow boundary condition results in lower LDL80 aortic surface area extensions. As observed previously (in particular by figures 3.2 and 3.3), the greater effects of the BC choice on LDL uptake at the luminal surface are showed by IC_F and IC_N cases, with a reduction of percentage LDL80 aortic surface area equal to 10.8% and 11.6%, respectively, when BC_{3D}, instead of BCF, is applied as inflow boundary condition.

To complete the analysis of the impact of BC-IC strategies on LDL concentration polarization the percentage value of the overlap of LDL80 aortic SA was evaluated, for every simulated case, considering the BC_{3D}-IC_{3D} strategy as the reference case (Figure 3.6).

It can be observed in figure 3.6 that the co-localization of LDL80 aortic surface areas between BC_{3D}-IC_{3D} and BC_{3D}-IC_F cases is equal to 78.3%, thus underlying a non-negligible role of initial conditions in determining the LDL lumen distribution. The imposition of IC_F, rather than IC_{3D}, as initial condition carries to a co-localization loss of 21.7%, when BC_{3D} is prescribes as inflow BC.

Figure 3.6 shows also that there is no co-localization, in terms of LDL80 aortic SA, between BC_{3D}-IC_{3D} and BC_{3D}-IC_U

cases. Moreover, there is no co-localization with BC_{3D}-IC_{3D} case if BC_F -IC_U is applied as BC-IC strategy.

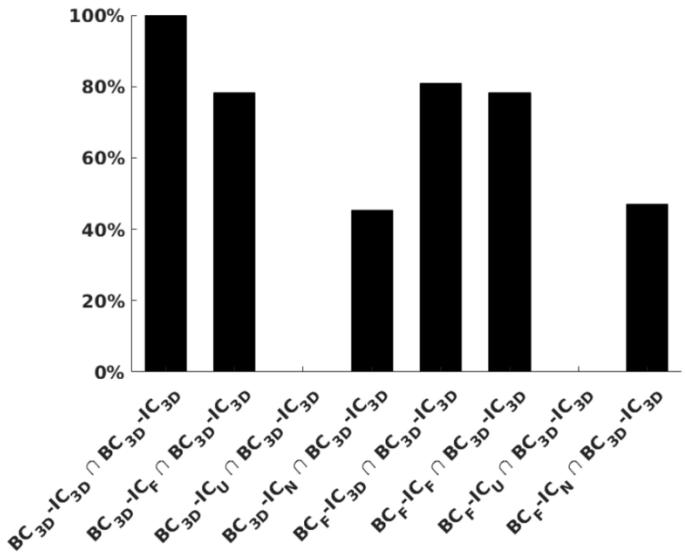

Figure 3.6 Quantitative analysis of the impact of BC-IC strategies on LDL concentration polarization: overlap of LDL80 aortic surface area, for all the applied BC-IC strategies, considering BC_{3D}-IC_{3D} as the reference case.

Investigating the role played by the imposed inflow boundary condition, when the same IC_{3D} condition is prescribed, obtained co-localization value of LDL80 surface areas between of BC_F with BC_{3D} case is 80.8%. More in detail, figure 6R highlights that the prescription of BC_F, rather than BC_{3D}, as inflow BC results in a co-localization loss equal

to 19.2%. Differences in co-localization of LDL80 aortic SA between BC_{3D}-IC_{3D} case and cases BC_{3D}-IC_N and BC_F-IC_N are equal to 45.4% and 47.1%, respectively, highlighting the effect of imposing IC_N as initial condition (Figure 3.6).

3.3 Co-localization of LDL80 and "disturbed" shear

The impact of modelling assumptions on simulated LDL transfer at the aortic wall was explored also analyzing the co-localization of luminal surface areas exposed to "disturbed" shear and LDL80. For cases with applied inflow BC_{3D} (more realistic) and BC_F, LDL80 vs. TAWSS20, OSI80, and RRT80 distributions and co-localization maps at the aortic luminal surface are presented in figure 3.7 and 3.8, respectively.

Displayed maps confirm that the application of different strategies of initial conditions results in different LDL polarization patterns (see also figure 3.2), identified by the red color in figures 3.7 and 3.8.

Comparing the two figures it also can be noticed the role played by the imposed inflow boundary condition in determining the extension of luminal surface areas TAWSS20, OSI80, and RRT80, indicated as the surface areas exposed to "disturbed" shear. In detail, looking at the blue

surface areas in the figures, it can be observed that the application of a flat velocity profile as inflow boundary condition leads to a marked overestimation of luminal surface areas TAWSS20 and RRT80.

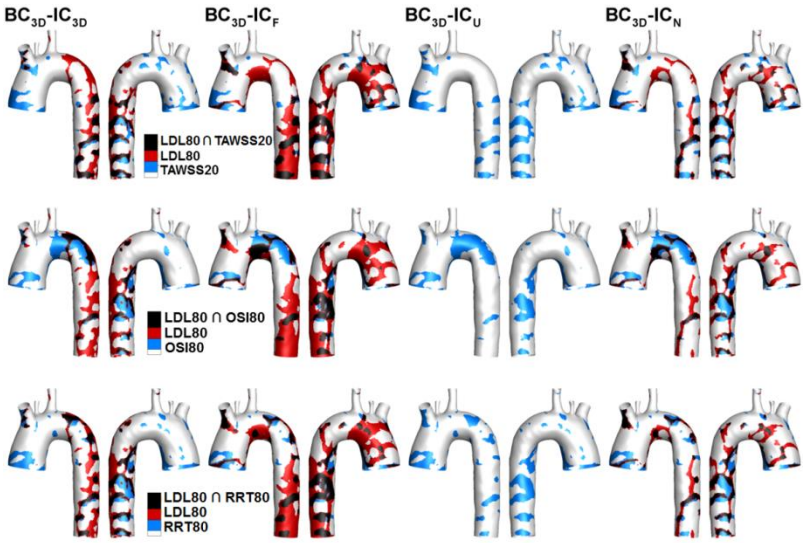

Figure 3.7 Distribution for the considered LDL80 concentration polarization profile at the aortic SA, and for WSS-based descriptors of disturbed shear TAWSS20, OSI80 and RRT80. Results from cases with applied inflow BC_{3D} and the four different LDL concentration ICs are presented. Regions at the luminal surface where LDL80 co-localizes with TAWSS20, OSI80, and RRT80 are also displayed.

Obtained results in terms of OSI80 aortic surface areas are slight less extended in BC_F cases with respect to BC_{3D} ones, independently of the applied initial condition.

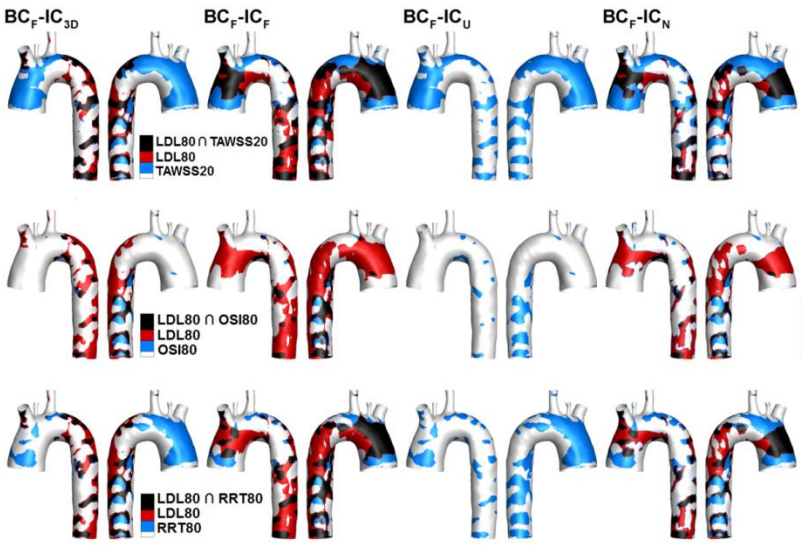

Figure 3.8 Distribution for the considered LDL80 concentration polarization profile at the aortic SA, and for WSS-based descriptors of disturbed shear TAWSS20, OSI80 and RRT80. Results from cases with applied inflow BC_F and the four different LDL concentration ICs are presented. Regions at the luminal surface where LDL80 co-localizes with TAWSS20, OSI80, and RRT80 are also displayed.

A more quantitative analysis for pairings LDL transfer to the aortic wall vs. TAWSS, OSI, and RRT descriptors, is presented in figures 3.9, 3.10 and 3.11, respectively.

Excluding the cases where IC_U is applied as initial condition (which result in zero co-localization), imposing both the investigated inflow boundary conditions (BC_{3D} and BC_F) result in IC-dependent values of co-localized SAs. In detail, differences in these values, for cases in which BC_{3D} is

applied as inflow BC, are up to: (1) 7.7% for LDL80 vs. TAWSS20; (2) 15.3% for LDL80 vs. OSI80; (3) 12.9% for LDL80 vs. RRT80. Instead, imposing the inflow BC_F results in IC strategy-dependent maximum differences in co-localized SAs: (1) 7.6% for LDL80 *vs.* TAWSS20; (2) 5.0% for LDL80 *vs.* OSI80; (3) 6.8% for LDL80 *vs.* RRT80.

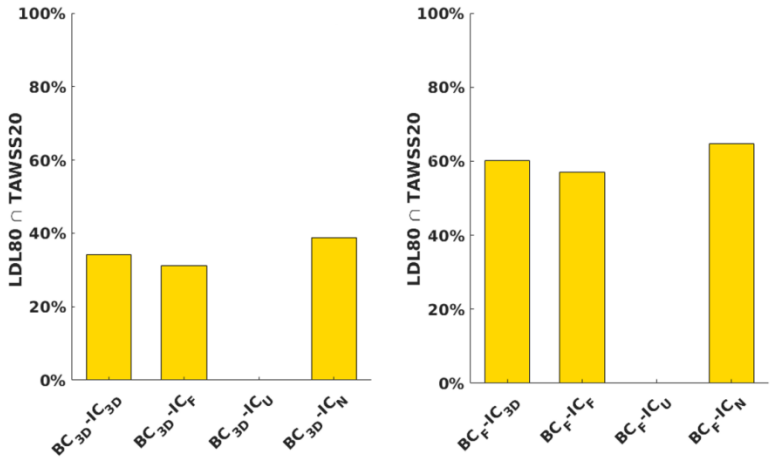

Figure 3.9 Percentage of aortic surface area where overlap occurs between LDL80 and TAWSS20. Results from cases with applied both inflow BC_{3D} (left) and BC_F (right), and the four different LDL concentration ICs are presented.

Investigating deeper the role played by the imposed inflow BC in determining the co-localized SAs for LDL80 *vs.* TAWSS20, it can be noticed that the prescription of BC_F, instead of BC_{3D}, results, with the exception of IC_U case, in an

increase of LDL80⋂TAWSS20 surface areas, independently of imposed initial condition (Figure 3.9). In detail, all cases are markedly affected by this overestimation of co-localized surface area, neglecting IC_U cases. Difference values between obtained results for BCF and BC3D cases, in terms of co-localized SAs for LDL80 *vs.* TAWSS20 are equal to 26%, 25.8% and 25.8% respectively when IC_{3D}, IC_F and IC_N are prescribed as initial conditions.

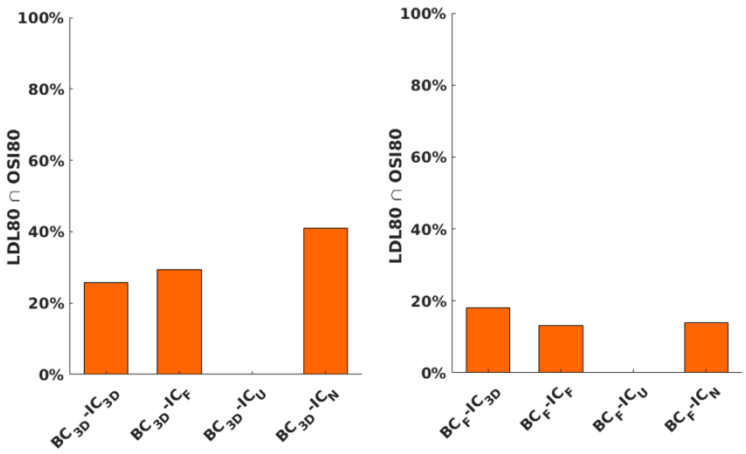

Figure 3.10 Percentage of aortic surface area where overlap occurs between LDL80 and OSI80. Results from cases with applied both inflow BC_{3D} (left) and BC_F (right), and the four different LDL concentration ICs are presented.

As concern the role played by the imposed inflow BC in the determination of co-localized SAs for LDL80 vs. OSI80,

the prescription of BC_F, instead of BC_{3D}, with the exception of ICU case, leads to a reduction of LDL80⋂OSI80 surface areas, independently of imposed initial condition (Figure 3.10). More in detail, the amount of this underestimation co-localized surface area, interesting all simulated cases neglecting the IC_U ones, is higher when IC_N is applied as initial condition and equal to 27.1%. Difference values between obtained results for BC_F and BC_{3D} cases, in terms of LDL80⋂OSI80 SAs are lower for IC3D and ICF cases and respectively equal to 7.7% and 16.3%.

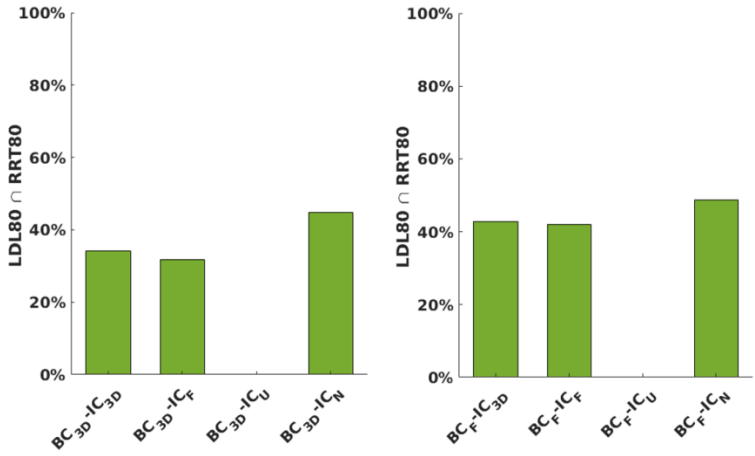

Figure 3.11 Percentage of aortic surface area where overlap occurs between LDL80 and RRT80. Results from cases with applied both inflow BC_{3D} (left) and BC_F (right), and the four different LDL concentration ICs are presented.

Regarding co-localized SAs for LDL80 vs. RRT80, as previously observed for the LDL80 vs. TAWSS20 overlapping, the prescription of BC_F, instead of BC_{3D}, as inflow boundary condition results, with the exception of IC_U case, in a slight overestimation of LDL80⋂RRT80 SAs, independently of imposed initial condition, as displayed by figure 3.11. Difference values between obtained results for BC_F and BC_{3D} cases, in terms of LDL80⋂RRT80 are lower (if compared with the ones obtained for LDL80⋂TAWSS20) and equal to 8.5%, 10.2% and 4.1% when IC_{3D}, IC_F and IC_N are prescribed as initial conditions, respectively.

To complete the analysis, the co-localization of aortic luminal surface areas characterized by high LDL transfer with descriptors of the complex multidirectional nature of WSS is visualized in figures 3.12 and 3.13, for cases in which BC_{3D} and BC_F are applied as inflow boundary condition, respectively.

In general, excluding the case where IC_U is applied (zero co-localization), prescribing the inflow BC_{3D} strategy results in co-localization of LDL80 aortic SA with SAs exposed to WSS_{ax}^{+} and WSS_{sc}^{rh} larger than WSS_{ax}^{-} and WSS_{sc}^{lh}, respectively (Figure 3.12). Moreover, pairing transWSS80 vs. LDL80 aortic SAs, they prove to be poorly co-localized with

respect to the other investigating parameters, independently of the applied IC.

When BC_F is applied as inflow BC, excluding the case where IC_U is prescribed (resulting again in null co-localized SAs), the overlap of LDL80 surface area with SAs exposed to WSS_{ax}^{-} and WSS_{sc}^{rh} larger than WSS_{ax}^{+} and WSS_{sc}^{lh}, respectively (Figure 3.13), highlighting the role played by imposed inflow BC in determining, in particular, WSS_{ax}. As concerns the co-localization of LDL80 aortic SA with transWSS80, they also prove to be slightly co-localized with respect to the other investigating parameters, independently of the applied IC.

A more quantitative analysis for pairings LDL transfer to the aortic wall vs. multidirectional WSS descriptors, is presented in figures 3.14, 3.15 and 3.16. In detail, figure 3.14 shows obtained percentage values of aortic surface areas where overlap occurs between LDL80 and each one of WSS_{ax}^{+} and WSS_{ax}^{-}, for all the eight simulated cases. It can be observed that, generally, the imposition of BC_{3D} as inflow boundary condition results in bigger co-localized surface areas of LDL80 and WSS_{ax}^{+}, compared to LDL80$\bigcap WSS_{ax}^{-}$ surface areas (except for IC_U case resulting in no co-localization). On the contrary, when inflow BC_F is prescribed, lower co-

localized surface areas of LDL80 and WSS_{ax}^{+}, compared to LDL80$\cap WSS_{ax}^{-}$ surface areas are obtained. Focalizing more the attention on the role played by the imposed inflow BC on co-localized SAs for LDL80 vs. WSS_{ax}^{+} (WSS_{ax}^{-}), it can be noticed that the prescription of BC_F, instead of BC_{3D}, as inflow boundary condition results, except for IC_U case, in a slight underestimation (overestimation) of LDL80$\cap WSS_{ax}^{+}$ (LDL80$\cap WSS_{ax}^{-}$) SAs, independently of imposed initial condition, as displayed by figure 3.14. Difference values between obtained results for BC_{3D} and BC_F cases, in terms of LDL80$\cap WSS_{ax}^{+}$ (LDL80$\cap WSS_{ax}^{-}$) are equal to 11.3% (- 11.3%), 8.7% (- 8.7%) and 4.5% (- 4.5%) when IC_{3D}, IC_F and IC_N are prescribed as initial conditions, respectively.

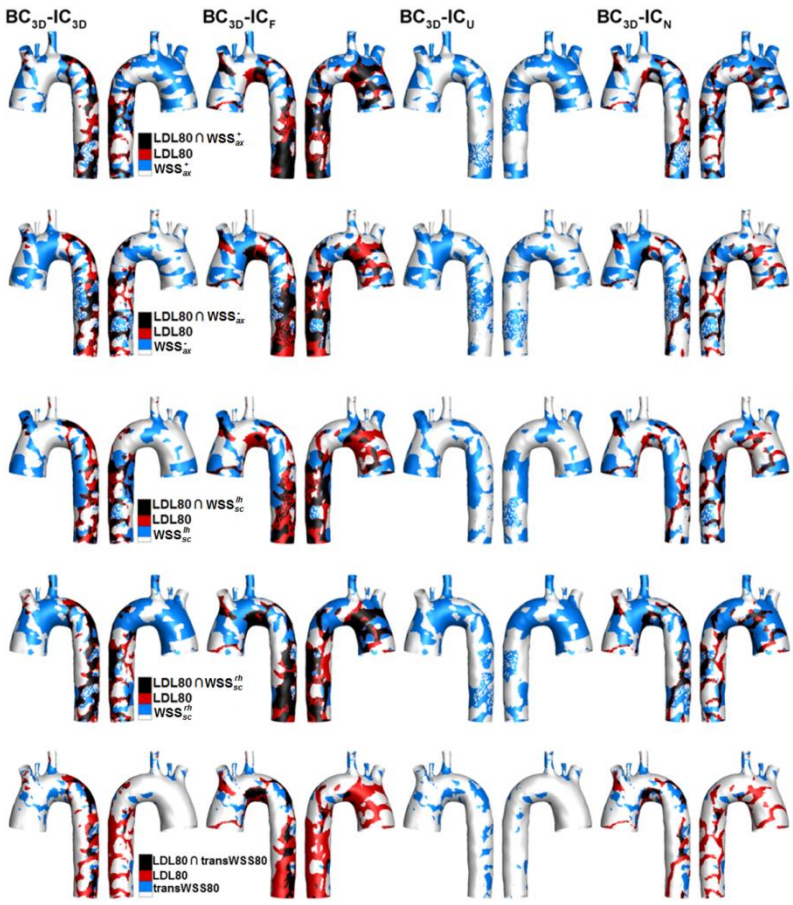

Figure 3.12 Distributions for the considered LDL80 concentration polarization profile at the aortic SA, and for multidirectional WSS descriptors WSS_{ax}^{+}, WSS_{ax}^{-}, WSS_{sc}^{lh}, WSS_{sc}^{rh} and transWSS80. Results from cases with applied inflow BC_{3D} and the four different LDL concentration ICs are presented. Regions at the luminal surface where LDL80 co-localizes with multidirectional WSS descriptors are also displayed.

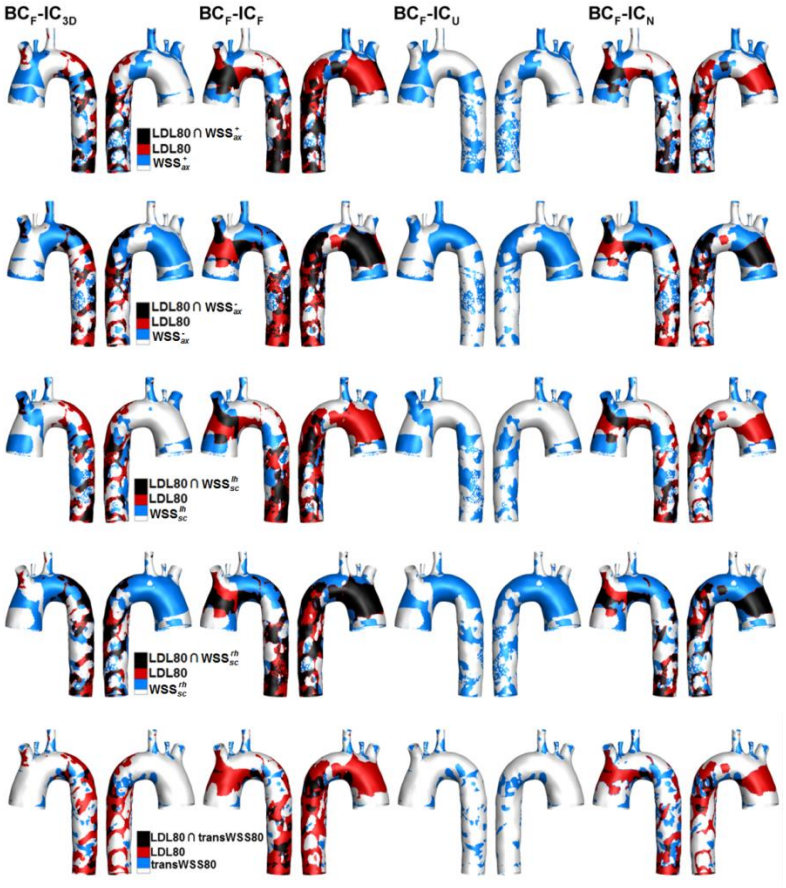

Figure 3.13 Distributions for the considered LDL80 concentration polarization profile at the aortic SA, and for multidirectional WSS descriptors $WSS_{ax}{}^{+}$, $WSS_{ax}{}^{-}$, $WSS_{sc}{}^{lh}$, $WSS_{sc}{}^{rh}$ and transWSS80. Results from cases with applied inflow BC_F and the four different LDL concentration ICs are presented. Regions at the luminal surface where LDL80 co-localizes with multidirectional WSS descriptors are also displayed.

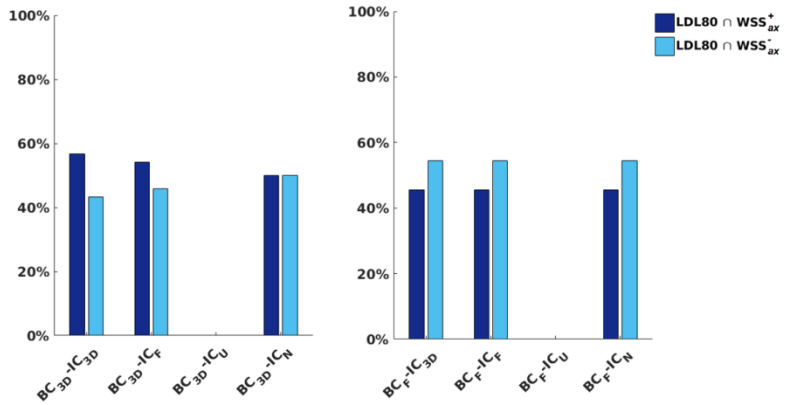

Figure 3.14 Percentage of aortic surface area where overlap occurs between LDL80 and each one of WSS_{ax}^{+} and WSS_{ax}^{-} (dark blue and light blue bars, respectively). Results from cases with applied both inflow BC_{3D} (left) and BC_F (right), and the four different LDL concentration ICs are presented.

Concerning the role of the LDL distribution prescribed as initial condition, figure 3.14 shows that IC_{3D} strategy results in a higher (lower) co-localized $LDL80 \cap WSS_{ax}^{+}$ ($LDL80 \cap WSS_{ax}^{-}$) surface areas, when inflow BC_{3D} is applied, whereas no IC-dependent effect can be observed when BC_F strategy is applied (with the exception of IC_U case).

Examining obtained results for the overlapping of (1) LDL80 and WSS_{sc}^{lh} SAs and (2) LDL80 and WSS_{sc}^{rh} SAs, displayed by figure 3.15, it can be noticed that, in general, both the investigated inflow BC results in co-localized

luminal surface areas of LDL80 and WSS_{sc}^{rh}, greater than LDL80⋂WSS_{sc}^{lh} surface areas. Except for the IC_U cases, again resulting in null co-localized surface areas, percentage values of LDL80⋂WSS_{sc}^{rh} are slightly higher for cases in which BC_F strategy is applied with a maximum absolute value of percentage difference equal to 11.6%, when IC_{3D} is prescribed. On the contrary LDL80⋂WSS_{sc}^{lh} assumes percentage values lower than the corresponding BC_{3D} case with a maximum, again when IC_{3D} is applied, equal to 10.5%.

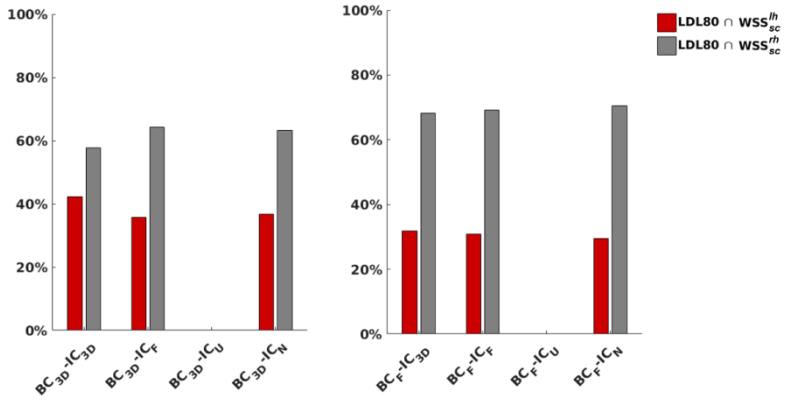

Figure 3.15 Percentage of aortic surface area where overlap occurs between LDL80 and each one of WSS_{sc}^{lh} and WSS_{sc}^{rh} (red and grey bars, respectively). Results from cases with applied both inflow BC_{3D} (left) and BC_F (right), and the four different LDL concentration ICs are presented.

As concerns as the role played by the imposed IC strategy in determining co-localization of (1) LDL80 and WSS_{sc}^{lh} and of (2) LDL80 and WSS_{sc}^{rh}, bar-charts in figure 3.15 exhibit, in general, a no IC-dependent trend for cases in which inflow BC_F strategy is applied for both the investigating overlapping surface areas; moreover, obtained percentage values for LDL80⋂WSS_{sc}^{lh} and LDL80⋂WSS_{sc}^{rh} SAs are slightly IC-dependent when inflow BC_{3D} is applied (except for IC_U case). The relative amount of investigating co-localized aortic surface areas, generally not changing among BC_F cases, varies between 14.3% and 28.5% (neglecting the IC_U case), when IC_{3D} and IC_F are prescribed, respectively.

To complete the analysis on co-localization of aortic luminal surface areas LDL80 with descriptors of the complex multidirectional nature of WSS, obtained results for the overlapping of LDL80 and transWSS80 are displayed by figure 3.16. As discussed above, comparing LDL80⋂transWSS80 resulting from the eight simulated cases, it can be noticed that the imposition of inflow BC_F, instead of BC_{3D}, carries to percentage difference values of SA up to 5.9% (for the IC_N case). Slightly IC-dependent trend of LDL80⋂transWSS80 aortic surface areas is highlighted by both bar-charts in figure 3.16, with more marked percentage

differences among results for BC_F cases up to 5% (again neglecting ICU case, resulting in null co-localized SA).

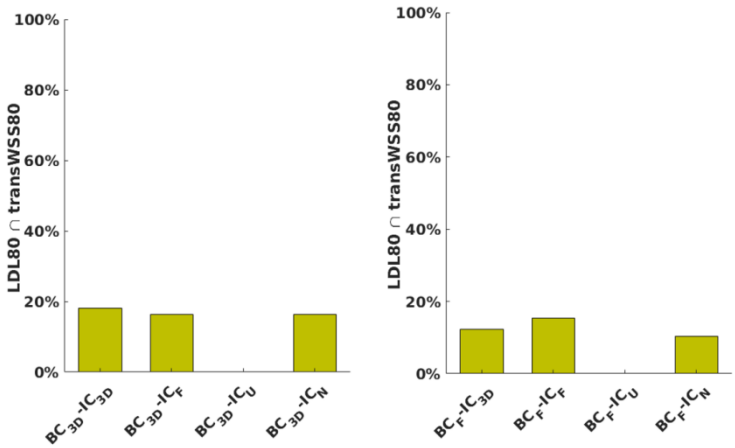

Figure 3.16 Percentage of aortic surface area where overlap occurs between LDL80 and transWASS80. Results from cases with applied both inflow BC_{3D} (left) and BC_F (right), and the four different LDL concentration ICs are presented.

3.4 Comparison of computed SA

Finally, in order to emphasize the impact of the imposed inflow boundary condition on determining luminal aortic TAWSS20, OSI80, RRT80, WSS_{ax}^{+}, WSS_{ax}^{-}, WSS_{sc}^{lh}, WSS_{sc}^{rh} and transWSS80 surface areas, percentage differences in those quantities, comparing obtained results for

BC_{3D}-IC_{3D} and BC_F-IC_{3D} cases, are reported by bar-chart in figure 3.17.

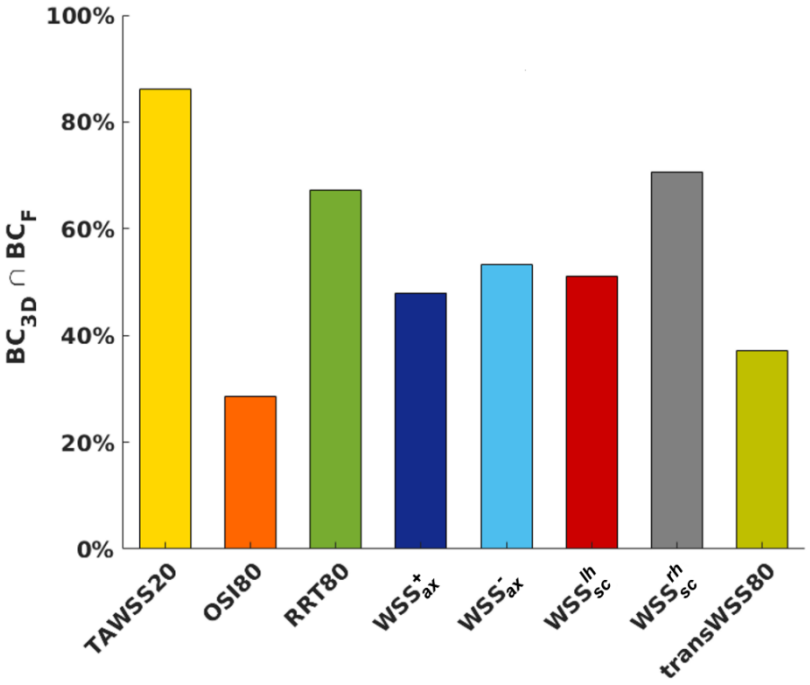

Figure 3.17 Percentage of co-localized aortic surface areas between IC_{3D} simulated cases. Results, in terms of luminal aortic TAWSS20, OSI80, RRT80, WSS_{ax}^{+}, WSS_{ax}^{-}, WSS_{sc}^{lh}, WSS_{sc}^{rh} and transWSS80 surface areas, obtained when BC_F is applied as inflow BC are compared with respect to the BC_{3D} case.

Figure 3.17 shows that the imposed BC plays a relevant role in determining luminal surface areas of "disturbed" shear. In

detail, the imposition of a flatvelocity profile at the inlet section of the aortic model results in a reduction to the 71.5% of the OSI80 luminal SA with respect to the case when BC_{3D} is applied as inflow BC. A significative variation in the extension of investigated SAs of "disturbed shear" can be observed also for WSS_{ax}^{+}, WSS_{ax}^{-}, WSS_{sc}^{lh} and transWSS80 surface areas. The percentage amount of differences in those quantities, for the comparing cases, are all greater than 47%, with a co-localization of 48%, 53%, 51% and 37%, respectively. Even if little lower, relevant differences can be obtained also computing TAWSS20, RRT80 and WSS_{sc}^{rh} SAs. The lowest values of percentage differences between the comparing cases are exhibited by the evaluation of TAWSS20, with the 86% of overlapping. However, it cannot be ignored that the imposition of an idealized (flat) velocity profile at the inlet section of the investigated domain, rather than a 3D measured one, lead to an overestimation, of 14% in amplitude, of the atheroprone aortic luminal surface area. Similar results are obtained for RRT80 aortic SA with an increase of the estimated luminal surface exposed to higher relative residence time of the 32.7% when BC_F is applied as inflow boundary condition (with respect to BC_{3D} case). Finally, obtained percentage differences in terms of estimated

WSS_{sc}^{rh} luminal SA, between the analysing cases, are of the 30%.

Chapter 4

Discussions and Conclusions

4.1 Discussions about the thesis project

Personalized aortic computational hemodynamics could represent a very useful tool in supporting the understanding of the low-density-lipoproteins transport and transfer role in atherogenic disease. However, the transport of the complex real problem under investigation in a computational/numerical one usually needs the making of some simplifying assumptions. The impact of these simplifications on the modelling of physiological aortic flow coupled with transport

phenomena in blood results in a source of uncertainty on obtained quantities, which has to be consider and assess to verify is can be neglected. In fact, the effect of the simplifying assumptions could affect the effectiveness of the constructed model to explain and replicate what really happens in human body.

In particular, LDL transport in aorta is characterized by high Peclet numbers, indicating the relative predominance of advective *vs.* diffusive transport. For this reason, it is expected that the applied inflow boundary condition influences not only the resulting flow field but also LDL transport in flowing blood and its blood-side to vessel wall transfer. Hence, the selection of the proper BC to prescribe at the inlet section of the investigating computational model assume a key role concerning results accuracy and reliability. Moreover, due to the common inability in obtaining personalized in vivo data of low-density lipoproteins concentration profiles over the arterial wall, it become crucial the evaluation of the impact that model assumptions based on arbitrary/deficitary measured data to properly set IC strategies.

This paucity of data, thwarting the increasing general attention paid to identify uncertainties stemming from assumptions in personalized computational hemodynamics, is

markedly limiting the establishment of rigorous, calibrated protocols for modelling LDL transfer which aim to balance the trade-offs among the variety of in vivo data to be acquired, CPU time, and the nominal accuracy required by the biological or clinical application.

This is confirmed by the body of literature dealing with LDL transfer modelling in arteries, indicating that in most studies the selection of the applied BC-IC strategy is scarcely documented, in particular the imposed initial wall distribution of LDL. Table 4.1 lists various studies investigating LDL transport in image-based aortic geometries. The provided overview of scientific studies is limited to the years 2011-2017. The list does not claim to be complete and exhaustive, but it is only useful in highlighting a deficit of documentation.

The reported studies are equally characterized by a lack in explicitly and clearly documenting the choice made for LDL wall distribution initialization. The absence of this information could affect the repeatability and reproducibility of the simulated phenomenon, at least in realistic computational hemodynamics aortic models. This aspect challenges the possibility to obtain reliable concentration profile estimation. The cumbersomeness of protocols and methods to properly modeling LDL transport in arterial

districts and its uptake at the arterial wall may prevent (1) to obtain reproducible and unambiguously comparable results among different laboratories and (2) to identify hemodynamics-based mechanistic criteria able to clarify the link between LDL transfer-to-wall and disturbed flow, and ultimately to atherogenesis.

As discussed in Chapter 1, indeed, reported studies investigate the effect on LDL transport and wall transfer in personalized model of human aorta of blood viscosity model (Liu et al, 2011; Soulis et al., 2016), turbulence model (Lantz and Karlsson, 2012) and model geometry (Chen et al., 2014; Lei et al., 2015), respectively. Researchers analyzed the relation between WSS (Soulis et al., 2014, 2016; Lei et al., 2015; Alimohammadi et al., 2016, 2017) or transmural pressure (Mpairaktaris et al., 2017) and mass transport.

Table 4.1: List of recent studies with focus on LDL transport in image-based aortic geometries

Authors	Title	Year of publication
Liu et al.	Effect of non-Newtonian and pulsatile blood flow on mass transport in the human aorta.	2011
Lantz and Karlsson	Large eddy simulation of LDL surface concentration in a subject specific human aorta.	2012
Chen et al.	Numerical investigation of mass transport through patient-specific deformed aortae	2014
Soulis et al.	Low Density Lipoprotein transport in the normal human aortic arch.	2014
Lei et al.	Influence of virtual intervention and blood rheology on mass transfer through thoracic aortic aneurysm.	2015
Alimohammadi et al.	Development of a patient-specific multi-scale model to understand atherosclerosis and calcification locations: comparison with *in vivo* data in an aortic dissection.	2016
Soulis et al.	Low density lipoprotein and non-Newtonian oscillating flow biomechanical parameters for normal human aorta.	2016
Alimohammadi et al.	A multiscale modelling approach to understand atherosclerosis formation: A patient-specific case study in the	2017

	aortic bifurcation.	
Li et al.	Numerical simulation of haemodynamics and low-density lipoprotein transport in the rabbit aorta and their correlation with atherosclerotic plaque thickness.	2017
Mpairaktaris et al.	Low density lipoprotein transport through patient-specific thoracic arterial wall.	2017

However, none has focused the attention on the proper definition of boundary and initial conditions for both fluid-dynamic and mass transport problems. In studies presented in this paragraph, indeed, several fluid-dynamic inflow boundary conditions have been applied. Researchers conducted (1) steady-state simulations by prescribing a flat (Liu et al., 2011; Chen et al., 2014; Soulis et al., 2014; Lei et al., 2015) or a parabolic (Mpairaktaris et al., 2017) inflow velocity profile and (2) unsteady-state simulations by applying a pulsatile flat velocity profile (Liu et al., 2011; Alimohammadi et al., 2016, 2017; Soulis et al., 2016) or not clearly declaring the imposed inflow velocity profile (Lantz and Karlsson, 2012). Regarding mass transport problem formulation, differences could be found in the definition of BC describing LDL diffusion across the vessel wall (i.e. by advection-diffusion equation or

permeability model). Imposed LDL BCs at model inlet and outlet surfaces are the same of this study (i.e. constant LDL concentration at inlet surface and stress free condition at outlets). All the presented studies are lacking in declaring prescribed initial LDL luminal concentration.

Results exposed in the previous chapter, in particular, testify to the impact that the application of different initial conditions, in terms of LDL distribution on the luminal aortic surface, has on transport of low-density lipoproteins in flowing blood and on their transfer to the aortic wall.

In this study, for the first time, the impact that both initial and inflow boundary conditions have in personalized computational model of human aortic LDL blood-to-wall transfer.

Even if the imposition of realistic 3D velocity profiles should always be preferable against idealized ones (as already demonstrated in Morbiducci et al., 2013), when 3D cine PC-MRI data are available, in most of the cases PC-MRI flow data from the clinical practice are made available only in terms of flow rate waveforms and not in terms of velocity profiles (in most of the cases flow rate values are based upon the acquisition of the sole through-plane phase velocity component at a vessel cross-section). The reason for this is

related to the fact that 3D cine PC-MRI is still not routinely applied in the clinical practice, mainly because of the longer acquisition times (still not fully compatible with the clinical practice). The consequence for this is that in most of the image-based computational hemodynamics studies the available PC-MRI measured flow rate waveforms must be applied as Dirichlet boundary condition at the inflow section(s) only in terms of idealized velocity profile, an assumption dictated by the lack of knowledge on the real profile associated to the measured flow rate.

In the future, when 3D PC-MRI will definitively be adopted in the clinical practice (recently developed acquisition settings already allow for parallel acquisition, with consequent speed up of the scanning time, see e.g., Volonghi et al., 2016), it will be easier to incorporate measured 3D velocity profiles within the computational framework.

Simulation results of this study have been analyzed in terms of computational costs, luminal SA exposing the highest LDL uptake and co-localization of high LDL uptake and atherogenic WSS patterns.

Concerning CPU time, the findings of this study highlight that prescribing realistic 3D measured velocity profiles as inflow BC is less computationally expensive than imposing

idealized velocity profiles, independently of the prescribed initial LDL wall distribution (Table 3.1). Moreover, the highest computational cost is obtained when IC_N is applied as LDL initial concentration at the vessel wall, independent of the inflow boundary condition. On the contrary, the lowest number of simulated cardiac cycles needed to damp the initial transient is shown by the application of BC_{3D}-IC_{3D} strategy (only 6 complete simulated cardiac cycles to reach the convergence condition).

As regards low-density lipoproteins accumulation at the arterial wall, huge differences have been reported by figure 3.1 comparing steady-state and unsteady-state simulation results, when the same BC-IC strategy is prescribed (BC_{3D}-IC_N). Obtained differences are in the order of 90-100% over all the aortic model surface proving the high amount of inaccuracy affecting steady-state simulations of LDL transport and wall transfer in aortic domain.

Focalizing the attention on resulting normalized cycle-averaged LDL concentration profiles at the luminal surface for the eight conducted unsteady-state simulations, figures 3.2, 3.3 and 3.6 highlight that it is lower and insensitive to the imposed inflow BC when a uniform initial condition is prescribed for the LDL wall distribution. Instead, the

application of an idealized velocity profile at the inlet section of the vascular model (BC_F) results in a larger LDL uptake, with respect to the BC_{3D} corresponding case. Table 3.2 and figure 3.4 show that the amount of the vessel wall interested by a greater LDL transfer when BC_F is applied as inflow, with respect to the BC_{3D} case, is higher that the 60%, independently of the imposed initial condition (the largest value, equal to 68%, is obtained when ICF is prescribed).

Analyzing results in terms of LDL80 aortic surface area, it emerge, with the exception of the IC_U case (LDL80 always equal to zero), that the application of different IC strategies produces less variability in those values when BC_{3D}, rather than BC_F, is prescribed at the inlet section of the model (Figure 3.5). However, both the imposed inflow boundary conditions produce appreciable variability (greater than 20%) in LDL80 SA with respect to the different imposed LDL wall distribution IC. Figure 3.6 investigates deeper this effect, induced by prescribed IC changing, by a co-localization analysis. It emerges that, even if the application of the inflow BC_{3D} carries to values of LDL80 luminal surface area less sensitive to the imposed IC, different BC_{3D}-IC strategies produce differently located polarization patterns, at the luminal surface (with a minimum value of co-localization

equal to 45.4% comparing case BC_{3D}-IC_N with the reference case, BC_{3D}-IC_{3D}). Moreover, among the imposed IC strategies, the application of an initial null LDL profile at the vessel wall affects more co-localization reported results.

In the absence of reference data for verification of the assumptions done to model aortic LDL transfer, the presumed link of LDL polarization patterns to disturbed shear is used for "consistency check" purposes. In particular, previous studies reported high LDL concentration values at low shear regions as a consequence, among others, of the weakened advective clearance from blood flow (Ethier, 2002; Sill et al., 1995; Sun et al., 2006). When considering the co-localization of LDL80 with SA exposed to atheroprone WSS, it emerges that when an inflow BC_{3D} is applied (with the exception of the IC_U case), LDL80 is poorly-to-moderately co-localized with TAWSS20, OSI80 and RRT80, with differences ascribable to the applied IC up to 15.3% (OSI80, figure 3.10). In the case of inflow BC_F, LDL80 co-localization is markedly larger with TAWSS20 and RRT80, and poorer with OSI80.

For each applied IC, differences in LDL80 *vs.* WSS-based descriptors co-localization between BC_{3D} and BC_F cases can be partially justified by the already observed sensitivity of

TAWSS20, OSI80 and RRT80 regions to the inflow velocity profile (Morbiducci et al., 2013).

Considering co-localization with descriptors of WSS multidirectionality (excluding again the IC_U case), it emerges that LDL80 is poorly co-localized with transWSS80 (co-localized SA lower than 20% of the aortic lumen surface area), for both cases in which inflow BC_{3D} or BC_F is applied. When an inflow BC_{3D} is applied maximum differences ascribable to the applied LDL concentration IC in WSS multidirectional phenotypes SA co-localized with LDL80 are about the half (7.6%, figures 3.14, 3.15 and 3.16), of the ones observed with OSI80. The imposition of an inflow BC_F has a relevant effect on the relative amount of co-localized SA between LDL80 and WSS_{ax}^{+} or WSS_{ax}^{-}, respectively, showing an inverse trend with respect to inflow BC_{3D} cases.

Figure 3.17, focusing on the impact of the imposed inflow BC on computed SAs, shows that the choice of the boundary condition to apply at the inlet section of the investigating domain has a no-neglecting effect on evaluating aortic lumen surface areas exposed to proatherogenic hemodynamic patterns. This effect results less marked on TAWSS20 and WSS_{sc}^{rh} SAs estimation, and it is more significant on computing OSI80 and transWSS80.

Several limitations could weaken the findings of this study. In particular, here it was assumed Newtonian behavior of blood, and neglected the shear dependence of LDL diffusivity (Sun et al., 2006). In this regard, recent studies in subject-specific computational hemodynamics models of healthy aorta show that "when compared to Newtonian blood flow simulation, the non-Newtonian behavior of blood has little effect on LDL transport in most parts of the aorta but could significantly affect those regions with high luminal surface LDL concentration by elevating C_W through the shear dependent diffusivity" (Liu et al., 2011).

The analysis is limited to only one clinical case, although the role played by geometry in affecting mass transport in computational model of human revealed by previous studies (Liu et al., 2009; Chen et al., 2014). However, preliminary results obtained on a second clinical case have identified the same main luminal areas of LDL polarization.

A further limitation is in the fact that here the analysis of LDL transport/transfer is restricted within the lumen, the LDL blood-to-wall transport being treated as a simple boundary condition. The blood-to-wall model instead of a multi-layer model is used in the present research. In detail, the most realistic approach to the problem of modeling mass

transport/transfer in arteries is to fully couple the transport within the lumen and the wall. This implies the need to model the transport within the wall (Moore and Ethier, 1997; Karner and Perktold, 2000; Karner et al., 2001; Stangeby and Ethier, 2002; Tarbell, 2003). In such cases the outer boundary of the computational domain is typically the medial-adventitial boundary. In this study, it was decided to focus the attention to the widely applied, less computationally expensive blood-to-wall transfer only modeling approach, in order to highlight that some assumptions related to BC-IC strategies could represent a source of uncertainty that we could classify as "unknown-unknowns". The fact that BC-IC strategies in LDL transport are "unknown-unknown" is reflected by a large body of literature and their impact seems to be not properly accounted for, thus limiting the reproducibility and comparability of the results among different labs.

As a consequence, the proposed modelling approach can be only applied to investigate the impact that hemodynamics has on LDL concentration profile, but it is unable to provide insights into the transport process of LDL inside the arterial wall.

Contrary to recent studies, here strategies to model turbulence were not applied, even if we are aware that the

presence of transitional flow in aorta could influence aortic LDL transport (Lantz and Karlsson, 2012). Moreover, arterial wall motion was neglected assuming rigid aortic model walls, even if aortic wall distensibility might influence local hemodynamics, and consequently LDL transport.

4.2 Conclusions of the thesis project

The findings of this study indicate that in modelling LDL transport and wall transfer in aorta, assumptions upon the inflow boundary condition and LDL concentration IC may have sensible impact on the modelled LDL blood-to-wall transfer. In detail, in the context of aortic LDL transfer and its link to atherosclerosis, it is observed that:

- attention should be put in setting idealized velocity profiles as inflow BC, because they may represent a source of uncertainty which is nonlinearly compounded by the uncertainty arising from assumptions (dictated by the lack of reference data) regarding the LDL concentration profile IC;
- different LDL concentration ICs produce different LDL concentration polarization profiles, independent of the applied inflow BC. Moreover, the imposition of

uniform LDL concentration profiles as IC (IC_U) may be inappropriate;

- different LDL concentration ICs imply markedly different computational costs;

It can be concluded that the imposition of 3D measured velocity profiles as inflow BC reduces the amount of uncertainty affecting the representation of the aortic LDL blood-to-wall transfer. Realistic 3D velocity profiles applied as aortic inflow BC has a not negligible impact on intravascular flow structures which appear to be different when idealized BCs are applied. Those marked differences in intravascular flow features have some reflection on LDL transport, form the results of this study.

Moreover, the imposition of LDL concentration profiles obtained by preliminary steady-state simulations as IC (in particular IC_{3D}) may capture LDL polarization profiles at the aortic wall with sufficient accuracy and acceptable computational cost.

In conclusion, given that it is not possible to verify in vivo the proper initial condition strategy to be applied, based on the findings of this study it has suggested (1) to carefully set and clearly and unambiguously declare the imposed LDL concentration IC in patient-specific computational models of

LDL transfer in aorta, with the final aim to obtain repeatable, reproducible and ultimately unambiguously comparable results among different laboratories.

The same level of attention is recommended when computational modelling of mass transport and wall transfer is performed in all realistic arterial geometries.

References

Alimohammadi, M., Pichardo-Almarza, C., Agu, O., Díaz-Zuccarini, V., 2016. *Development of a patient-specific multi-scale model to understand atherosclerosis and calcification locations: comparison with in vivo data in an aortic dissection.* Frontiers in Physiology, 7:238.

Alimohammadi, M., Pichardo-Almarza, C., Agu, O., Díaz-Zuccarini, V., 2017. *A multiscale modelling approach to understand atherosclerosis formation: A patient-specific case study in the aortic bifurcation.* Proceedings of the Institution of Mechanical Engineers H 231, 378-390.

Allender, S., Scarborough, P., O'Flaherty, M., Capewell, S., 2008. *Patterns of coronary heart disease mortality over the 20th century in England and Wales: Possible plateaus in the rate of decline*. BMC Public Health 8, 148.

Antiga, L., Piccinelli, M., Botti, L., Ene-Iodarche, B., Remuzzi, A., Steinmann, D.A., 2008. An image-based modelling framework for patient-specific computational hemodynamics. Medical and Biological Engineering and Computing 46 (11), 1097-1112.

Bijari, P.B., Antiga, L., Gallo, D.,Wasserman, B.A., Steinman, D.A., 2012. *Improved prediction of disturbed flow via hemodynamically-inspired geometric variables.* Journal of Biomechanics 45(9),1632-7.

Bratzler, B.L., Chisolm, G.M., Colton, C.K., Smith, K.A., Lees, R.S., 1977. *The distribution of labeled low-density lipoproteins across the rabbit thoracic aorta in vivo.* Arteriosclerosis 28, 289-307.

Brown, M.S., Goldstein, J.L., 1983. *Lipoprotein metabolism in the macrophage: implications for cholesterol deposition in atherosclerosis.* Annual Review of Biochemistry 52, 223-64.

Brown, M.S., Goldstein, J.L., 1986. *A receptor-mediated pathway for cholesterol homeostasis.* Science 232(4746), 34-47.

Brown, A.G., Yubing, S., Marzo, A., Staicu, C., Valverde, I., Beerbaum, P., Lawford, P.V., Hose, D.R., 2012. *Accuracy vs. computational time: translating aortic simulations to the clinic.* Journal of Biomechanics 45, 516–523.

Caro, C.G., Fitz, G.J., Schroter, R.C., 1969. *Arterial wall shear and distribution of early atheroma in man.* Nature 223, 1159-1160.

Caro, C.G., Fitzgerald, J.M., Schroter, R.C., 1971. *Atheroma and arterial wall shear. Observation, correlation and*

proposal of a shear dependent mass transfer mechanism for atherogenesis. Proceedings of the Royal Society of London B: Biological sciences 177, 109-159.

Carroll, G.T., Devereux, P.D., Ku, D.N., McGloughlin, T.M., Walsh M.T., 2010. *Experimental validation of convection-diffusion discretisation scheme employed for computational modelling of biological mass transport.* Biomedical Engineering Online 9:34.

Chen, J., Gutmark, E., Mylavarapu, G., Backeljauw, P.F., Gutmark-Little, I., 2014. *Numerical investigation of mass transport through patient-specific deformed aortae.* Journal of Biomechanics 47, 544-552.

Deng, X., King, M., Guidoin, R., 1993. *Localization of atherosclerosis in arterial junctions. Modeling the release rate of low density lipoprotein and its breakdown products accumulated in blood vessel walls.* ASAIO Journal (American Society for Artificial Internal Organs) 39, M489-M495.

Deng, X., Marois, Y., How, T., Merhi, Y., King, M., Guidoin, R., Karino, T., 1995. *Luminal surface concentration of lipoprotein (LDL) and its effect on the wall uptake of cholesterol by canine carotid arteries.* Journal of Vascular Surgery 21, 135-145.

Ethier, C.R., 2002. *Computational modeling of mass transfer and links to atherosclerosis.* Annals of Biomedical Engineering 30, 461-471.

Friedman, M.H., Hutchins, G.M., Bargeron, C.B., Deters, O.J., Mark F.F., 1981. *Correlation between intimal thickness and fluid shear in human arteries.* Atherosclerosis 39, 425-36.

Galbraith, C.G., Skalak, R., Chien, S., 1998. *Shear Stress induces spatial reorganization of the endothelial cell cytoskeleton.* Cell Motility and the Cytoskeleton 40, 317-330.

Gallo, D., De Santis, G., Negri, F., Tresoldi, D., Ponzini, R., Massai, D., Deriu, M.A., Segers, P., Verhegghe, B., Rizzo, G., Morbiducci, U., 2012. *On the Use of in vivo measured flow rates as boundary conditions for image-based hemodynamic models of the human aorta. Implications for indicators of abnormal flow.* Annals of Biomedical Engineering 40, 729-741.

Gallo, D., Steinman, D.A., Morbiducci, U., 2016. *Insights into the co-localization of magnitude-based versus direction-based indicators of disturbed shear at the carotid bifurcation.* Journal of Biomechanics 49, 2413-2419.

Getz, G.S., 1990. *An overview of atherosclerosis: a look to the future.* Toxicologic Pathology 18, 623-635.

Glagov, S., Zarins, C., Giddens, D.P., Ku, D.N., 1988. *Hemodynamics and atherosclerosis, insights and perspective gained from studies of human arteries.* Archives of Pathology and Laboratory Medicine 112, 1018-1029.

Goldstein, J.L., Ho, Y.K., Basu, S.K., Brown M.S., 1979. *Binding site on macrophages that mediates uptake and degradation of acetylated low density lipoprotein, producing massive cholesterol deposition.* Proceedings of the National Academy of Sciences 76(1), 333-7.

Gray, H., 1918. *Anatomy of the Human Body.* Philadelphia: Lea & Febiger, 1918

He, X., Ku, D.N., 1996. *Pulsatile flow in the human left coronary artery bifurcation: average conditions*. ASME Journal of Biomechanical Engineering 118(1),74-82.

Heinecke, J.W., Rosen, H., Chait, A., 1984. *Iron and copper promote modification of low density lipoprotein by human arterial smooth muscle cells in culture.* Journal of clinical investigation 74(5), 1890-4.

Henriksen, T., Mahoney, E.M., Steinberg, D., 1981. *Enhanced macrophage degradation of low density lipoprotein previously incubated with cultured endothelial cells: recognition by receptors for acetylated low density lipoproteins.* Proceedings of the National Academy of Sciences 78(10), 6499–6503.

Himburg, H.A., Grzybowski, D.M., Hazel, A.L., LaMack, J.A., Li, X.M., Friedman, M.H., 2004. *Spatial comparison between wall shear stress measures and porcine arterial endothelial permeability.* American Journal of Physiology Heart and Circulatory Physiology 286, H1916–H1922.

Hoi, Y., Wasserman, B.A., Lakatta, E.G., Steinman, D.A., 2010. *Effect of common carotid artery inlet length on normal carotid bifurcation hemodynamics.* ASME Journal of Biomechanical Engineering 132, 121008.

Kang, H., Cancel, L.M., Tarbell, J.M., 2014. *Effect of shear stress on water and LDL transport through cultured endothelial cell monolayers.* Atherosclerosis 233, 682-90.

Karner, G., Perktold, K., 2000. E*ffect of endothelial injury and increased blood pressure on albumin accumulation in the arterial wall: a numerical study.* Journal of Biomechanics 33, 709–715

Karner, G., Perktold, K., Zehentner, H.P., 2001. *Computational modeling of macromolecule transport in the arterial wall.* Computer Methods in Biomechanics and Biomedical Engineering 4, 491–504

Kilner, P.J., Yang, G.Z., Mohiaddin, R.H., Firmin, D.N., Longmore, D.B., 1993. *Helical and retrograde secondary flow patterns in the aortic arch studied by three-directional magnetic resonance velocity mapping.* Circulation 88, 2235–2247.

Ku, D.N., Giddens, D.P., Zarins, C.K., Glagov, S., 1985. *Pulsatile flow and atherosclerosis in the human carotid bifurcation. Positive correlation between plaque location and low and oscillating shear stress.* Arteriosclerosis 5, 293-302.

Ku, D.N., Giddens, D.P., Zarins, C.K., Glagov, S., 1985. *Pulsatile flow and atherosclerosis in the human carotid bifurcation. Positive correlation between plaque location and low and oscillating shear stress.* Atherosclerosis 5 (3), 293-302.

Ku, D.N., 1997. *Blood flow in arteries.* Annual Review of Fluid Mechanics 29, 399-434.

Kumar, V., Butcher, S.J., Öörni, K., Engelhardt, P., Heikkonen, J., Kaski, K., Ala-Korpela, M., Kovanen, P.T., 2011. *Three-Dimensional cryoEM Reconstruction of Native LDL Particles to 16Å Resolution at Physiological Body Temperature*. PLoS ONE 6(5), e18841.

Lantz, J., Karlsson, M., 2012. *Large eddy simulation of LDL surface concentration in a subject specific human aorta.* Journal of Biomechanics 45, 537-542.

Lee, S.W., Antiga, L., Spence, J.D., Steinman, D.A., 2008. *Geometry of the carotid bifurcation predicts its exposure to disturbed flow.* Stroke 39, 2341–2347.

Lee, S.W., Antiga, L., Steinman, D.A., 2009. *Correlations among indicators of disturbed flow at the normal carotid bifurcation.* ASME Journal of Biomechanical Engineering 131(6), 061013, 7 pp.

Lei, Y., Chen, M., Xiong, G., Chen, J., 2015. *Influence of virtual intervention and blood rheology on mass*

transfer through thoracic aortic aneurysm. Journal of Biomechanics 48, 3312-3322.

Leuprecht, A., Kozerke, S., Boesiger, P., Perktold, K., 2003. *Blood flow in the human ascending aorta: a combined MRI and CFD study*. Journal of Engineering Mathematics 47, 387-404.

Lever, M.J., Tarbell, J.M., Caro, C.G., 1992. *The effect of luminal flow in rabbit carotid artery on transmural fluid transport.* Experimental Physiology 77, 553-563.

Li, X., Liu, X., Zhang, P., Feng, C., Sun, A., Kang, H., Deng, X., Fan, Y., 2017. *Numerical simulation of haemodynamics and low-density lipoprotein transport in the rabbit aorta and their correlation with atherosclerotic plaque thickness.* Journal of the Royal Society, Interface 14, pii20170140.

Liu, X., Pu, F., Fan, Y., Deng, X., Li, D., Li, S., 2009. *A numerical study on the flow of blood and the transport of LDL in the human aorta: the physiological significance of the helical flow in the aortic arch.* American Journal of Physiology Heart and Circulatory Physiology 297, H163-H170.

Liu, X., Fan, Y., Deng, X., Zhan, F., 2011. *Effect of non-Newtonian and pulsatile blood flow on mass transport in the human aorta.* Journal of Biomechanics 44, 1123-1131.

Malek, A.M., Alper, S.L., Izumo, S., 1999. *Hemodynamic shear stress and its role in atherosclerosis.* JAMA 282, 2035-2042.

Marzo, A., Singh, P., Reymond, P., Stergiopulos, N., Patel, U., Hose, R., 2009. *Influence of inlet boundary conditions on the local haemodynamics of intracranial aneurysms.* Computer Methods in Biomechanics and Biomedical Engineering 12, 431–444

Morbiducci, U., Ponzini, R., Rizzo, G., Cadioli, M., Esposito, A., DeCobelli, F., Del Maschio, A., Montevecchi, F.M., Redaelli, A., 2009. *In vivo quantification of helical blood flow in human aorta by time-resolved three-dimensional cine phase contrast MRI.* Annals of Biomedical Engineering 37, 516–531.

Morbiducci, U., Ponzini, R., Rizzo, G., Cadioli, M., Esposito, A., Montevecchi, F.M., Redaelli, A., 2011. *Mechanistic insight into the physiological relevance of helical blood flow in the human aorta: an in vivo study*. Biomechanics and Modeling in Mechanobiology 10, 339-355.

Morbiducci, U., Ponzini, R., Gallo, D., Bignardi, C., Rizzo, G., 2013. *Inflow boundary conditions for image-based computational hemodynamics: impact of idealized versus measured velocity profiles in the human aorta.* Journal of Biomechanics 46, 102-109.

Morbiducci, U., Gallo, D., Cristofanelli, S., Ponzini, R., Deriu, M.A., Rizzo, G., Steinman, D.A., 2015. *A*

rational approach to defining principal axes of multidirectional wall shear stress in realistic vascular geometries, with application to the study of the influence of helical flow on wall shear stress directionality in aorta. Journal of Biomechanics 48, 899-906.

Morel, D.W., Di Corleto, P.E., Chisolm, G.M., 1984. *Endothelial and smooth muscle cells alter low density lipoproteins in vitro by free radical oxidation.* Arteriosclerosis 4, 357-64.

Moore, J.A., Ethier, C.R., 1997. *Oxygen Mass Transfer Calculations in Large Arteries.* ASME Journal of Biomechanical Engineering 119, 469-475.

Mpairaktaris, D.G., Soulis, J.V., Giannoglou, G.D., 2017. *Low density lipoprotein transport through patient-specific thoracic arterial wall.* Computers in Biology and Medicine 89, 115-126.

Musliner, T.A., Krauss, R.M., 1988. *Lipoprotein subspecies and risk of coronary disease.* Clinical Chemistry 34, B78-83.

Napoli, C., D'Armiento, F.P., Mancini, F.P., Postiglione, A., Witztum, J.L., Palumbo, G., Palinski, W., 1997. *Fatty streak formation occurs in human fetal aortas and is greatly enhanced by maternal hypercholesterolemia*. Journal of Clinical Investigation 100, 2680-90.

Nerem, R., 1995. *Atherosclerosis and the role of wall shear stress.* In Flow dependent Regulation of Vascular Function, ed. JA Bevan, G Kaley, GM Rubany. New York: Oxford University Press.

Nielsen, LB., 1996. *Transfer of low density lipoprotein into the arterial wall and risk of atherosclerosis.* Atherosclerosis 123, 1-15.

Pedersen, E.M., Agerbaek, M., Kristenses, I.B., Yoganathan, A.P., 1997. *Wall shear stress and early atherosclerosis lesions in the abdominal aorta in young adults.* European Journal of Vascular and Endovascular Surgery 13, 443-451.

Peiffer, V., Sherwin, S.J., Weinberg, P.D., 2013. *Computation in the rabbit aorta of a new metric - the transverse wall shear stress - to quantify the multidirectional character of disturbed blood flow*. Journal of Biomechanics 46, 2651-2658.

Reymond, P., Merenda, F., Perren, F., Rufenacht, D., Stergiopulos, N., 2009. *Validation of a one-dimensional model of the systemic arterial tree.* American Journal of Physiology Heart and Circulatory Physiology 297, H208–H222

Schneck, D.J., 1995. *An outline of cardiovascular structure and function*, in The biomedical engineering handbook. Ed. Bronzino, CRC Press Inc., Hartford (CT), USA.

Shaaban, A.M., Duerinckx, A.J., 2000. *Wall shear stress and early atherosclerosis: a review*. America Journal of Roentgenology 74, 1657-1665.

Sill, H.W., Chang, Y.S., Artman, J.R., Frangos, J.A., Hollis, T.M., Tarbell, J.M., 1995. *Shear-stress increases hydraulic conductivity of cultured endothelial monolayers.* American Journal of Physiology Heart and Circulatory Physiology 268, H535-H543.

Soulis, J., Dimitrakopoulou, M., Giannoglou, G., 2014. *Low Density Lipoprotein transport in the normal human aortic arch*. Hippokratia 18, 221-225.

Soulis, J.V., Fytanidis, D.K., Lampri, O.P., Giannoglou, G.D., 2016. *Low density lipoprotein and non-Newtonian oscillating flow biomechanical parameters for normal human aorta.* Cardiology Research 7, 66-79.

Stangeby, D.K., Ethier, C.R., 2002. *Computational Analysis of Coupled Blood-Wall Arterial LDL Transport*. ASME Journal of Biomechanical Engineering, 24(1), 1-8.

Stary, H.C., Chandler, A.B., Glagov, S., Guyton, J.R., Insull, W. Jr, Rosenfeld, M.E., Schaffer, S.A., Schwartz, C.J., Wagner, W.D., Wissler, R.W., 1994. *A definition of initial, fatty streak, and intermediate lesions of atherosclerosis.* A report from the Committee on Vascular Lesions of the Council on Arteriosclerosis, American Heart Association. Circulation 89, 2462-2478.

Steinberg, D., Parthasarathy, S., Carew, T.E., Khoo, J.C., Witztum, J.L., 1989. *Beyond Cholesterol. Modifications of low-density lipoprotein that increase its atherogenicity.* New England Journal in Medicine 320, 915-924.

Sun, N., Wood, N.B., Hughes, A.D., Thom, S.A., Xu, X.Y., 2006. *Fluid-wall modelling of mass transfer in an axisymmetric stenosis. Effects of shear-dependent transport properties.* Annals of Biomedical Engineering 34, 1119-1128.

Tada, S., 2010. *Numerical study of oxygen transport in a carotid bifurcation.* Physics in Medicine and Biology 55, 3993-4010.

Tarbell, J.M., 2003. *Mass transport in arteries and the localization of atherosclerosis.* Annual Review of Biomedical Engineering 5, 79-118.

Truskey, G.A., Roberts, W.L., Herrmann, R.A., Malinauskas, R.A., 1992. *Measurement of endothelial permeability to 125I-low density lipoproteins in rabbit arteries by use of en face preparations.* Circulation Research 71, 883-897.

Vincent, P.E., Weinberg P.D., 2014. *Flow-dependent concentration polarization and the endothelial glycocalyx layer: multi-scale aspects of arterial mass transport and their implications for atherosclerosis.* Biomechanics and Modeling in Mechanobiology 13, 313-326.

Volonghi, P., Tresoldi, D., Cadioli, M., Usuelli, A.M., Ponzini, R., Morbiducci, U., Esposito, A., Rizzo, G., 2016. *Automatic extraction of three-dimensional thoracic aorta geometric model from phase contrast MRI for morphometric and hemodynamic characterization.* Magnetic Resonance in Medicine 75, 873-882.

Wada, S., Karino, T., 1999. *Theoretical study on flow-dependent concentration polarization of low density lipoproteins at the luminal surface of a straight artery.* Biorheology 36, 207-223.

Wada, S., Karino, T., 2002. *Theoretical prediction of low-density lipoproteins concentration at the luminal surface of an artery with a multiple bend.* Annals of Biomedical Engineering 30, 778-791.

Wen, C., Yang, A., Tseng, L., Chai, J., 2010. *Investigation of pulsatile flowfield in healthy thoracic aorta models.* Annals of Biomedical Engineering 38, 91–402.

Witztum, J.L., Steinberg, D., 1991. *Role of oxidized low density lipoprotein in atherogenesis.* Journal of Clinical Investigation 88(6),1785-92.

Wootton, D.M., Ku, D.N., 1999. *Fluid mechanics of vascular systems, diseases, and thrombosis.* Annual Review of Biomedical Engineering 1, 299-329.

Yang, N., Vafai, K., 2006. *Modeling of low-density lipoprotein (LDL) transport in the artery-effects of*

hypertension. International Journal of Heat and Mass Transfer 49, 850-867.

Zhang, D.W., Garuti, R., Tang, W.J., Cohen, J.C., Hobbs, H.H., 2008. *Structural requirements for PCSK9-mediated degradation of the low-density lipoprotein receptor*. Proceedings of the National Academy of Sciences of the United States of America 105 (35): 13045–13050.

Zhang, Q., Steinman, D.A., Friedman, M.H., 2010. *Use of factor analysis to characterize arterial geometry and predict hemodynamic risk: application to the human carotid bifurcation.* ASME Journal of Biomechanical Engineering, 132:114505.

POLITECNICO
DI TORINO

ScuDo
Scuola di Dottorato – Doctoral School
WHAT YOU ARE, TAKES YOU FAR

UNIVERSITÀ
DEGLI STUDI
DI TORINO